Final Project Report

DE-SC0001280

Characterizing the Combined Roles of Iron and Transverse Mixing on Uranium Bioremediation in Groundwater using Microfluidic Devices

PIs:	Kevin T. Finneran, Clemson University and Charles Werth, University of Texas at Austin, Timm Strathmann, University of Illinois at Urbana-Champaign (moving to Colorado School of Mines in January 2015)
Science Element:	Subsurface Biogeochemistry
DOE/Office of Science Program:	Environmental Remediation Science Program
DOE/Program Office Contact:	Dr. Roland Hirsch

Rationale for this Project

In situ bioremediation of U(VI) involves amending groundwater with an appropriate electron donor (and any other limiting nutrients) to promote biological reduction to the less soluble and mobile U(IV) oxidation state. Groundwater flow is laminar; mixing is controlled by hydrodynamic dispersion. Recent studies indicate that transverse dispersion along plume margins can limit mixing of the amended electron donor and accepter (such as U(VI) in remediation applications). As a result, microbial growth, and subsequently contaminant degradation, may be limited to these transverse mixing zones during bioremediation. A variety of electron donors have been shown to promote reduction of U(VI) to U(IV). These include acetate, lactate, H_2, ethanol, Fe(II), and possibly hydroquinones. In the absence of iron, microbial growth is expected to occur only in the region where the electron donor and U(VI) mix through transverse dispersion. In the presence or Fe(III), microbial growth occurs not only in the transverse mixing zone, but also in regions where Fe(II) is generated. This is expected because the electron donor reduces Fe(III) to Fe(II), and sorbed Fe(II) species can subsequently reduce U(VI) to U(IV). Since Fe(II) will only be produced where electron donor is present, the transverse region of growth may grow if excess Fe(II) diffuses transverse to the direction of flow over time. As a result, U(VI) reduction kinetics is expected to be faster, and occur over larger regions, in the presence of iron. How biotic and abiotic reduction processes contribute to these processes was not clear at the onset of this work.

Also, it was not clear how biomass and U(IV) and/or Fe(II) precipitates affect transverse mixing, and subsequent rates of U(VI) reduction. As Fe(III) and U(VI) reduction proceed the surface(s) of the biomass may become coated in precipitates such as uraninite ($UO_{2(s)}$) or siderite ($FeCO_{3(s)}$). The mixing inhibition promoted by these surface precipitates may inhibit further U(VI) reduction, such that the process becomes self-limiting over time. We were able to monitor the production of precipitates along with the biomass within the pore network, and characterize the mineralogy of some of the solids.

Re-oxidation of U(IV) has been observed in sediment when oxic or nitrate-bearing water is re-introduced to the system and the electron donor concentration is too low to maintain reduction of all electron acceptors. There are several reports of pure or enrichment cultures as well that re-oxidize U(IV) to U(VI) with nitrate as the electron acceptor. Fe(II) oxidation,

alternatively, is primarily an abiotic reaction at circumneutral pH. Although Fe(II) is a biological electron donor for lithotrophic organisms, it is quickly oxidized to Fe(III) by oxygen and the kinetics of the abiotic reaction is significantly faster than the biological reaction. However, when nitrate is the electron acceptor, the dominant Fe(II) oxidation pathway is biotic. As a result, U(IV) is expected to readily oxidize to soluble U(VI) along plume margins when electron donor amendment ceases, and nitrate-reducing or oxic conditions return to the system. In the presence of iron, oxidation of U(IV) is expected to lag behind the oxidation of adsorbed Fe(II) on the surface of the biofilm and possibly throughout the biofilm.

In the completed work, transverse mixing zones along plume margins were re-created in microfluidic pore networks, hereafter referred to as micromodels. While investigation of transverse mixing zones in larger scale flow-cells is possible, our recent work indicated that the transverse width of microbial growth can be on the order of a few pore bodies. Micromodels also offered the advantage that their surfaces can be coated with a variety of metal oxides, including silicon and iron oxides, and their pore dimensions can be exactly controlled. We conducted a series of experiments that allowed us to distinguish among the hydraulic, biological, and geochemical mechanisms that contribute to U(VI) reduction, U(IV) re-oxidation, U(VI) precipitation with the limiting biological nutrient phosphorous (as HPO_4^{2-}). This systematic approach may lead to a better understanding of U(VI) bioremediation, and better strategies for electron donor amendment to maximize bioremediation efficiency.

Technical Significance

The work expanded the current state of knowledge in the field of uranium bioremediation and biogeochemistry by determining the combined influence of hydraulics, biology, and geochemistry on uranium precipitation. The DOE has supported a number of investigators examining uranium bioremediation. The projects have expanded to the point where specific microbial communities have been identified, specific influences and amendments have been investigated in situ, and individual reaction mechanisms have been elucidated. The highly controlled and detailed investigations described below will allow practitioners to develop in situ uranium bioremediation strategies where processes can be adequately modeled prior to the first amendments being added. To allow this kind of accuracy in situ, however, the specific reaction mechanisms and kinetics must be defined correctly to prevent the application of unsuccessful strategies at individual sites.

Objectives and Hypotheses

The primary objective of this work was to characterize the combined effects of hydrology, geochemistry, and biology on the (bio)remediation of U(VI). Our underlying hypothesis was that bioremediation of U(VI) in groundwater is controlled by transverse mixing with an electron donor along plume margins, and that iron bioavailability in these zones affects U(VI) reduction kinetics and U(IV) re-oxidation. Our specific objectives were to a) quantify reaction kinetics mediated by biological versus geochemical reactions leading to U(VI) precipitation, UV(VI) reduction and U(IV) re-oxidation, b) understand the influence of bioavailable iron on U(VI) reduction and U(IV) re-oxidation along the transverse mixing zones, c) determine how transverse mixing limitations and the presence of biomass or mineral precipitates in pores affects these reactions, and d) identify how microbial populations that develop along transverse mixing zones are influenced by the presence of iron and the concentration of electron donor.

Methods and Scope of Work

Overview. Our general approach was to divide the work into distinct tasks associated with the micromodel experiments. All tasks 1-3 used a pure culture with highly-controlled, defined chemistry micromodels. We targeted U(VI) reduction in micromodels with and without Fe(III) present. We also studied abiotic U(IV) precipitation in the presence of phosphate. The influence of electron donor (concentration and duration of amendment) as well as abiotic reactions with sulfides or reduced hydroquinones in the presence and absence of Fe(III) was investigated in batch studies.

All experiments were conducted under strict anaerobic conditions using established laboratory procedures. Specialized procedures and equipment were also used to avoid sample exposure to air outside of anaerobic glovebox environments. In experiments where oxic water was introduced to micromodels, the water injected had approximately 8.0mg/L dissolved oxygen, but the micromodels were still maintained in an anoxic environment. All aqueous samples were collected using an anaerobic syringe and needle; solid samples were collected inside of a glovebox chamber or using a modification of the Hungate technique.

Micromodel Description. Microfluidic pore structures developed in our previous work were used to address the specific aims, so the synthesis and basic analysis methods are detailed here. For synthesis of microfluidic pore structures, digitized images of a periodic and aggregate pore structures were previously transferred to chrome-platted glass masks. Each mask served as a template to transfer the image via ultra-violet light exposure to a silicon wafer coated with photoresist. The exposed photoresist was removed with a developer, and then the imprinted pore structure was etched into silicon using inductively coupled plasma – deep reactive ion etching (ICP-DRIE). After etching, the pore structure was either exposed to air at 1000^{o}C to develop a silicon dioxide layer on the surface, or subjected to DC magnetron sputtering to create an iron oxide layer. The oxygen content and temperature during sputtering were tailored to create a-Fe_2O_3 (hematite). After being flushed with buffered water it was expected to become at least partially $Fe(OH)_3$, poorly crystalline Fe(III) (hydr)oxide. Selected locations of the pore network were coated with a-Fe_2O_3 by re-coating the pore network with photoresist and developing only the areas to be coated before sputtering. Both silicon and iron oxide layers were hydrophilic and have surface properties similar to those of silicate and iron mineral oxides found in soil and groundwater sediments. After creation of the oxide layers, glass was anodically bonded to the etched pore structure surface. The bonded pore structure was then was placed into an aluminum manifold equipped with ultra-low dead volume connection ports to deliver and carry away fluid. A photograph of a microfluidic device loaded into a flow manifold is shown in the attached manuscript.

We evaluated microbial growth and U(VI) precipitation with phosphate in micromodels with a homogeneous pore network consisting of a periodic array of cylinders; an SEM image of this pore structure is shown in the attached manuscript. Pores in these structures were characterized by a variety of water velocities and shear, and were expected to cause changes in the locations of substrate mixing and growth along the transverse mixing zone. Each pore structure had two inlets and inlet channels, and one outlet and outlet channel. This allowed us to introduce two parallel and adjacent water streams (e.g., 1 with U(VI), 1 with e^- donor) into the microfluidic pore structure and to set up a transverse mixing zone. Each inlet was fed from a separate syringe pump to achieve an average linear velocity, *v*, of 0.1 cm/min (~20 ml/hour), expect where noted otherwise. This flow rate was representative of those found in sandy aquifers, and growth occurred in a reasonable time period (i.e., within weeks) at this velocity.

For biotic experiments, growth substrates were introduced into the microfluidic pore structure for a period of 5-20 days. The culture used was the environmentally relevant *Geobacter metallireducens,* and we expected it to attach to micromodel surfaces and grow in the microfluidic pore structures. After inoculation, each microfluidic device was purged via the inlets as described below to stimulate growth and U(VI) reduction along the transverse mixing zone. Reflected light differential interference contrast (DIC) microscopy was used to image the location of total biomass in the pore structures. Epifluorescent microscopy was used to monitor the distribution of specific organisms and activity as detailed under each specific aim.

For abiotic experiments, U(VI) was introduced into one inlet of the micromodel, and HPO_4^{2-} was introduced into the other. In separate experiments, calcium (Ca^{2+}) or sulfate (SO_4^{2-}) was introduced into both inlets with U(VI) and HPO_4^{2-} to evaluate the effect on U(VI) precipitation. Precipitation was allowed to progress for up to 35 hours, and the morphology of precipitates, crystals formed, and effect on mixing was evaluated. As before, reflected DIC microscopy was used to image the location of precipitates in the pore structures. Epifluorescent microscopy was used to monitor fluid flow, and Raman spectroscopy was used to identify crystals formed.

Controls were run for all biological experiments and included: buffer alone, U(VI) alone (no electron donor amendment), and electron donor alone (no U(VI) amendment. The controls were not separate micromodels that ran simultaneously, but rather controls that were run prior to the onset of the full suite of experimental conditions. For example; U(VI)-only controls were run for several days prior to adding cells or electron donor and the effluent was monitored for changes in U(VI). Once we had data demonstrating no U(VI) loss in the absence of cells plus electron donor, we added the cells plus electron donor or chemical amendments and continued the experiment. This method was used for all controls, as the total number of micromodels that can be synthesized and run was limited.

Results of this Project

General findings regarding microfluidic devices

1. Microfluidic devices were constructed using etched silica or etched silica on which ferric iron was sputtered; x-ray diffraction analysis demonstrated that the dominant form of Fe(III) present on the surfaces of the micromodel posts was hematite.
2. "Solid phase iron"-free microfluidic devices were used to assess the rate and extent of biomass development when *Geobacter metallireducens* was inoculated with acetate and Fe(III) citrate as the electron donor/acceptor pair meeting and mixing along the transverse mixing line within the micromodels. Initial experiments were failures in that the cells were added initially at too high a concentration and the biomass grew along the inlet chambers, essentially blocking all flow through the microfluidic devices. This is shown in Figure 1 below

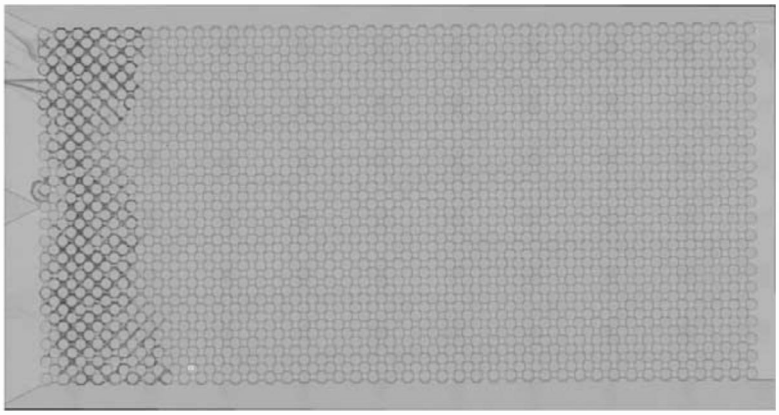

Figure 1. Dense growth of Geobacter metallireducens in the micromodel pore structure.

We re-assessed biomass inoculation and switched to a strategy where a resting cell suspension, diluted to low biomass (10^4-10^5 cells per mL) was inoculated into the system prior to the onset of adding electron donor or electron acceptor. Cells developed along the transverse mixing line in the expected orderly manner, in which biomass was greater near the influent ports and became more dilute at the distal end of the chamber. This is shown in Figure 2 below.

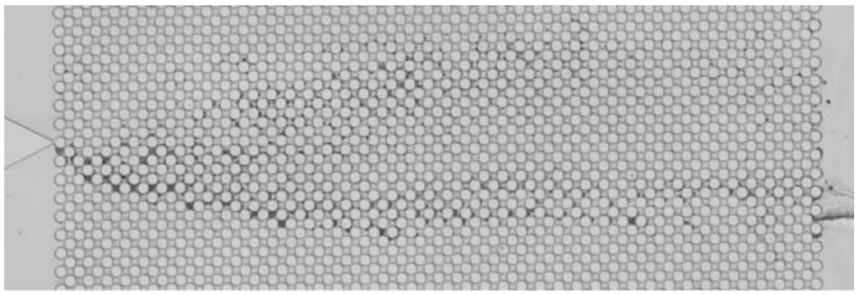

Figure 2. Growth of Geobacter metallireducens along the central mixing zone of the micromodel pore structure.

3. Studies done with Raman spectroscopy indicated that the mass accumulating on the posts was biomass, as peaks for all major biomolecules were present. The biomass

developed in a manner consistent with flow through the posts (pore spaces) – the biomass was high on the leading edge of the flow and sheared as the pore throats decreased; biofilms on the downgradient edge of the flow (posts) tailed off, consistent with how water is expected to move through these pore spaces. A Raman spectra showing biomass developed in the pore structure is shown in Figure 3 below.

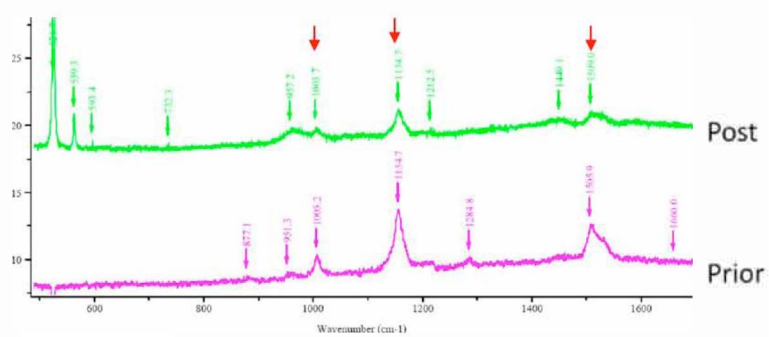

Figure 3. Raman backscattering spectroscopy of biomass grown in micromodel. The peaks at 1004 and 1155 cm^{-1} are assigned to aromatic structures in the cell membrane, which are fairly stable to laser excitation. The peak at 1509 cm^{-1} can be assigned to nucleic acids, which are destroyed under laser light at this wavelength.

4. U(VI) was tested as the sole electron acceptor and does support growth, in the expected manner along the transverse mixing line; however, issues with uranyl phosphate precipitation confounded interpretation of results, and led to a series of experiments investigating the mineral phases that result during phosphorus mediated uranyl precipitation.
5. U(VI) precipitation in the presence of HPO_4^{2-} occurred over the time scale of hours to days. Relative to when only U(VI) and HPO_4^{2-} were present, precipitation rates were 2.3 times slower when SO_4^{2-} was present, and 1.4 times faster when Ca^{2+} was present; larger crystals formed in the presence of SO_4^{2-}. Raman backscattering spectroscopy and micro-X-ray diffraction results both showed that the only mineral precipitated was chernikovite, UO_2HPO_4 - $4H_2O$; energy dispersive X-ray spectroscopy results indicate that Ca and S are not incorporated into the chernikovite lattice. A pore-scale model was developed, and simulation results of saturation ratio (SR = Q/Ksp) suggest that chernikovite is the least thermodynamically favored mineral to precipitate ($0 < SR < 1$) compared to uranyl hydrogen phosphate and Na-autunite ($13 < SR < 40$), and uranyl orthophosphate and Ca-autunite (when Ca^{2+} is present; $SR > 105$). Fluorescent tracer studies and laser confocal microscopy images showed that densely aggregated precipitates blocked pores and reduced permeability. The results suggest that uranium precipitation with phosphate as chernikovite is rapid on the time scale of remediation for the conditions considered and can block pores, alter fluid flow paths, and potentially limit mixing and precipitation.

A manuscript detailing the results is attached.

General findings using batch experiments for aqueous uranium

1. Experiments were conducted with uranyl adsorption on ferrihydrite versus aluminum oxide to assess the capacity for microorganisms and extracellular electron shuttling compounds to directly reduce U(VI) adsorbed to the surface of oxide solids. Initial data demonstrated that 99% of the U(VI) remains adsorbed (in HEPES buffered solution) and up to 90-95% of the adsorbed U(VI) can be recovered in solution when extracted with

bicarbonate buffer. The next phase of the experiments introduced the hydroquinone to characterize whether adsorbed U(VI) can be reduced directly, or whether Fe(III)/Fe(II) is necessary to catalyze U(VI) reduction. U(VI) was not reduced in the attached (adsorbed) form based on the specific buffer used.

2. The hydroquinone reduced U(VI) at greater than 90% reduced in the aqueous phase in HEPES buffer; in 30mM bicarbonate buffer aqueous U(VI) it was not reduced.
3. Adsorbed U(VI) on both aluminum and iron acts in the same manner; HEPES buffered suspensions were readily reduced, while bicarbonate buffered suspensions are not reduced to a significant extent.
4. The role of HEPES versus bicarbonate is being investigated further as this will affect future experiments run by DOE investigators .

WATER RESOURCES RESEARCH, VOL. 49, 874–890, doi:10.1002/wrcr.20088, 2013

Pore-scale evaluation of uranyl phosphate precipitation in a model groundwater system

Michael F. Fanizza,[1] Hongkyu Yoon,[2] Changyong Zhang,[3] Martinus Oostrom,[3] Thomas W. Wietsma,[3] Nancy J. Hess,[3] Mark E. Bowden,[4] Timothy J. Strathmann,[1] Kevin T. Finneran,[5] and Charles J. Werth[1]

Received 7 May 2012; revised 18 December 2012; accepted 30 December 2012; published 16 February 2013.

[1] The abiotic precipitation of uranium (U(VI)) was evaluated in a microfluidic pore network (i.e., micromodel) to assess the efficacy of using a phosphate amendment to immobilize uranium in groundwater. U(VI) was mixed transverse to the direction of flow with hydrogen phosphate (HPO_4^{2-}), in the presence or absence of calcium (Ca^{2+}) or sulfate (SO_4^{2-}), in order to identify precipitation rates, morphology and types of minerals formed, and effects of mineral precipitates on pore blockage. Precipitation occurred over the time scale of hours to days. Relative to when only U(VI) and HPO_4^{2-} were present, precipitation rates were 2.3 times slower when SO_4^{2-} was present, and 1.4 times faster when Ca^{2+} was present; larger crystals formed in the presence of SO_4^{2-}. Raman backscattering spectroscopy and micro-X-ray diffraction results both showed that the only mineral precipitated was chernikovite, $UO_2HPO_4 \cdot 4H_2O$; energy dispersive X-ray spectroscopy results indicate that Ca and S are not incorporated into the chernikovite lattice. A pore-scale model was developed, and simulation results of saturation ratio ($SR = Q/K_{sp}$) suggest that chernikovite is the least thermodynamically favored mineral to precipitate ($0 < SR < 1$) compared to uranyl hydrogen phosphate and Na-autunite ($13 < SR < 40$), and uranyl orthophosphate and Ca-autunite (when Ca^{2+} is present; $SR > 10^5$). Fluorescent tracer studies and laser confocal microscopy images showed that densely aggregated precipitates blocked pores and reduced permeability. The results suggest that uranium precipitation with phosphate as chernikovite is rapid on the time scale of remediation for the conditions considered and can block pores, alter fluid flow paths, and potentially limit mixing and precipitation.

Citation: Fanizza, M. F., H. Yoon, C. Zhang, M. Oostrom, T. W. Wietsma, N. J. Hess, M. E. Bowden, T. J. Strathmann, K. T. Finneran, and C. J. Werth (2013), Pore-scale evaluation of uranyl phosphate precipitation in a model groundwater system, *Water Resour. Res.*, *49*, doi:10.1002/wrcr.20088.

1. Introduction

[2] Contamination of groundwater and soil with uranium has resulted from anthropogenic activities such as uranium mining and milling and processing of uranium for nuclear weapons and energy programs [*Wolbarst et al.*, 1999; *National Research Council (NRC)*, 2010], as well as from natural processes in rock, soil, and water. Uranium contamination causes health risks and presents serious public health concerns [*Zimmerman et al.*, 2007; *NRC*, 2008]. A great deal of resources has been directed toward identifying efficient in situ strategies to remove soluble U(VI) from groundwater, including promotion of in situ biological reduction (see summaries in *Fang et al.* [2009] and *Dunham-Cheatham et al.* [2011]), and abiotic reactions including adsorption and mineral precipitation [*Morrison and Spangler*, 1992; *Naftz et al.*, 1996; *Gabriel et al.*, 1998; *United States Environmental Protection Agency (USEPA)*, 2000; *Simon and Biermann*, 2005; *Wellman et al.*, 2008; *Hiemstra et al.*, 2009]. Among these approaches, abiotic precipitation has received considerable attention due to its success in uranium removal from soil and groundwater [*Arey et al.*, 1999; *USEPA*, 2000; *Fuller et al.*, 2002; *Simon et al.*, 2008].

[3] A variety of U(VI) mineral precipitates has been observed at sites where anthropogenic activities and/or weathering resulted in the release of uranium to the environment, and in associated laboratory studies. Near several uranium mines (Apex Mine, Nevada, and Midnite Mine,

[1]Department of Civil and Environmental Engineering, University of Illinois at Urbana-Champaign, Urbana, Illinois, USA.
[2]Geomechanics Department, Sandia National Laboratories, Albuquerque, New Mexico, USA.
[3]Fundamental and Computational Sciences Directorate, Pacific Northwest National Laboratory, Richland, Washington, USA.
[4]Environmental Molecular Sciences Laboratory, Pacific Northwest National Laboratory, Richland, Washington, USA.
[5]Department of Environmental Engineering and Earth Sciences, Clemson University, Clemson, South Carolina, USA.

Corresponding author: C. J. Werth, University of Illinois at Urbana-Champaign, Department of Civil and Environmental Engineering, 205 N Mathews, Urbana, IL 61801, USA. (werth@uiuc.edu)

0043-1397/13/10.1002/wrcr.20088

Washington) where sulfate is present, the mineral uranopilite [$(UO_2)_6SO_4(OH)_{10} \cdot 12H_2O$] was found [*Frost et al.*, 2007]. Near the Coles Hill U deposit in Virginia, Ba uranyl phosphate (Ba meta-autunite, [$Ba(UO_2)_2(PO_4)_2 \cdot nH_2O$]) is present [*Jerden and Sinha*, 2003; *Jerden et al.*, 2003; *Jerden and Sinha*, 2006]. In the vicinity of a secondary uranium ore deposit at Koongarra, Australia, both Mg meta-autunite [$Mg(UO_2)_2(PO_4)_2 \cdot nH_2O$] and nanocrystals of metatorbernite [$Cu(UO_2)_2(PO_4)_2 \cdot 8H_2O$] were identified [*Murakami et al.*, 1997, 2005]. At the Hanford site in Washington, several silicon-containing U(VI) minerals were identified in the vadose zone directly above the water table, i.e., uranophane-type phases [$Ca(UO_2)_2(SiO_3OH)_2(H_2O)_5$] [*Um et al.*, 2010] and sodium boltwoodite [$Na(UO_2)(SiO_3OH) \cdot 1.5H_2O$] [*Catalano et al.*, 2004], as well as a copper-containing mineral below a discharge pond, i.e., metatorbernite [$Cu(UO_2)_2(PO_4)_2 \cdot 8H_2O$] [*Arai et al.*, 2007]. The facultative anaerobe *Rahnella* sp. Y9602, isolated from soil at the Oak Ridge Field Research Center, was used to release orthophosphate by hydrolysis of glycerol-3-phosphate and promote abiotic precipitation of chernikovite [$UO_2HPO_4 \cdot 4H_2O$] [*Beazley et al.*, 2009]. In the presence of Ca^{2+}, chernikovite can form the more stable mineral Ca meta-autunite [$Ca(UO_2)_2(PO_4)_2 \cdot nH_2O$] via ion exchange [*Martinez et al.*, 2007], i.e., the replacement of hydrogen in two unit cells of chernikovite with Ca^{2+}. Among the aforementioned mineral phases, those containing phosphate have received the most attention because they are stable under oxic conditions (e.g., in contrast to UO_2), their precipitation rates are generally faster, and/or their solubilities are generally lower near circumneutral pH compared to nonphosphate-containing minerals; they are the focus of this effort.

[4] Phosphate has been amended as natural apatite materials (e.g., phosphate rock, bone meal, and bone meal charcoal), including the mineral hydroxylapatite (HAP) [$Ca(PO_4)_3OH$], in batch and column studies [*Fuller et al.*, 2002; *Arey et al.*, 1999; *Simon et al.*, 2008] and in a permeable reactor barrier (PRB) wall [*Fuller et al.*, 2003; *USEPA*, 2000]. In batch and column studies with low uranium concentrations (e.g., <7 mg U(VI) g HAP^{-1}), immobilization occurred through U(VI) sorption to the HAP or natural apatite materials (e.g., bone char) [*Fuller et al.*, 2002, 2003; *Simon et al.*, 2008], not U(VI) precipitation. However, for higher U(VI) concentrations (e.g., 5500 mg U(VI) g bone $char^{-1}$), and in the absence of dissolved carbonate, X-ray diffraction (XRD) results indicated that uranium precipitated with phosphate as chernikovite, autunite, and/or saleeite [$Mg(UO_2PO_4)_2 \cdot 10H_2O$] [*Fuller et al.*, 2002, 2003; *Simon et al.*, 2008]. Uranium precipitation can be inhibited in the presence of dissolved carbonate due to the formation of highly soluble uranyl carbonate complexes [e.g., $Ca_2UO_2(CO_3)_{3(aq)}$] [*Fuller et al.*, 2003]. In Fry Canyon, Utah, a PRB wall containing a natural apatite material (i.e., bone char) was used to remove U(VI) in the presence of approximately 4.8 m*M* total dissolved carbonate [*USEPA*, 2000]. Uranium in groundwater was reduced from as high as approximately 4.7 mg L^{-1} to as low as 0.06 mg L^{-1}. Sorbed uranium concentrations in recovered bone char were as high as 690 μg U(VI) g^{-1}. XRD and XAS (X-ray adsorption spectroscopy) were used to analyze reactive barrier wall material posttreatment, and no uranium precipitates were observed. In batch studies, similar results were obtained using the same materials and conditions, but precipitates were observed when carbonate was removed [*Fuller et al.*, 2003]. This indicates that uranium removal occurred primarily by U(VI) sorption through surface complexation with apatite surfaces, and U(VI) precipitation as phosphate minerals is inhibited by the presence of dissolved carbonates.

[5] To overcome phosphate limitations associated with solid phase apatites, aqueous phase phosphate has been directly used to precipitate uranium from water in batch studies, amended to groundwater and uranium impacted Hanford sediments in batch and column studies [*Fuller et al.*, 2002], and amended to a uranium impacted groundwater aquifer at Pacific Northwest National Laboratory's Hanford site (300 area) in Washington state [*Wellman et al.*, 2007; *Vermeul et al.*, 2009]. In the batch study containing only water, phosphate was added by first equilibrating water with apatite, and then the aqueous phase with phosphate was separated from apatite and amended with equimolar amounts of uranium [*Fuller et al.*, 2002]. Chernikovite precipitation occurred when phosphate and uranium concentrations each exceeded 100 μ*M*. In batch studies with Hanford groundwater and sediments, multiple phosphate sources were evaluated, including sodium salts of orthophosphate, pyrophosphate, tripolyphosphate, trimetaphosphate, and hexametaphosphate and calcium salts of dihydrogen phosphate, hydrogen phosphate, and pyrophosphate [*Vermeul et al.*, 2009]. The sodium salts of orthophosphate, pyrophosphate, and tripolyphosphate resulted in the most uranium sequestration, and sequestration increased in the presence of calcium chloride. In column studies containing Hanford groundwater and sediments, polyphosphates and calcium were sequentially flushed through the column and used to sequester uranium. Posttreatment analysis of the sediments using short-wave UV radiation (254 nm) showed fluorescent green precipitates were present, indicative of uranium phosphate minerals. Similar to batch and column studies, uranium sequestration was also observed in Hanford 300 area groundwater after polyphosphate addition. Mineral precipitation was indicated by changes in permeability, suggesting pore blockage, but no mineralogical data are available to assess removal mechanisms. In none of these studies, mineral precipitation rates were evaluated, and the effect of phosphate mineral precipitation on pore blockage was not further evaluated. Hence, it is not clear if phosphate addition under mixing limited conditions in groundwater resulted in uranium precipitation, or if mixing limitations prevented widespread precipitation and resulted in pore blockage.

[6] The objectives of this work were to quantify uranyl phosphate precipitation rates at the pore scale under representative flow, mixing, and geochemical conditions, the corresponding effects of selected groundwater ions on these rates, the type and morphology of uranium minerals that precipitate, and the resulting pore blockage. Uranium precipitation with phosphate was promoted along a transverse mixing zone in a microfluidic pore network (i.e., micromodel) in the presence and absence of calcium and sulfate ions. Precipitation rates were quantified using brightfield reflected microscopy images, and mineral phases and compositions were evaluated in situ using Raman backscattering spectroscopy and ex situ using micro-X-ray diffraction

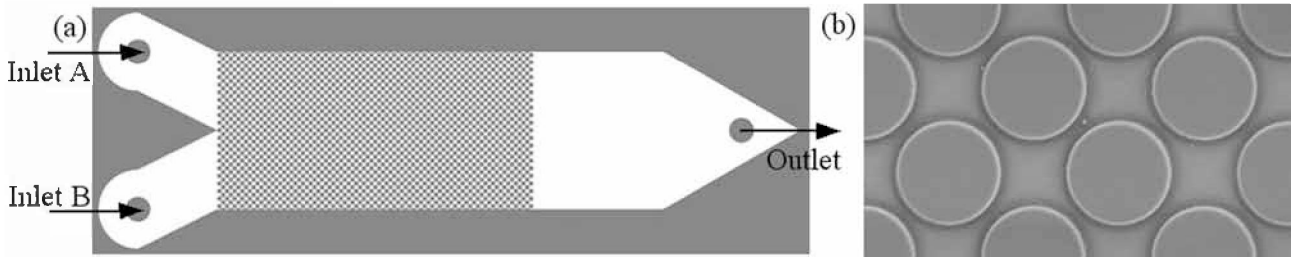

Figure 1. (a) Schematic of micromodel with labeled inlets and outlets and (b) pore structure with a homogeneous array of pores. The pore structure in (a) is 2 cm long by 1 cm wide. The individual grains in (b) are 300 μm in diameter.

(μ-XRD), environmental scanning electron microscopy (SEM), and energy dispersive spectroscopy. Pore blockage was evaluated using scanning confocal microscopy and breakthrough of a fluorescent tracer. The effects of calcium and sulfate were examined because they are common groundwater constituents, and because they are found in U(VI) minerals identified at several important field sites. A pore-scale reactive transport model with U speciation was used to evaluate the effects of pore-scale reactive transport on dominant U species in the pore space, and the degree of saturation with respect to different U(VI)-phosphate mineral phases. To our knowledge, this is the first study of uranium phosphate precipitation in a flow cell amenable to direct visualization and analysis of mineral precipitates and is the first direct comparison of experimental precipitates with pore-scale reactive transport model predictions. The unique approach allows us to test the hypotheses that the solution conditions (i.e., the presence of Ca^{2+} and SO_4^{2-}) affect the type of minerals formed during precipitation, and the precipitation rate, morphology, and effects on flow and mixing.

2. Materials and Methods

2.1. Materials

[7] Uranyl nitrate ($UO_2(NO_3)_2$, Fluka), sodium phosphate dibasic (Na_2HPO_4, Sigma-Aldrich), calcium chloride ($CaCl_2$, Sigma-Aldrich), sodium sulfate (Na_2SO_4, Sigma-Aldrich), and fluorescein (70%, Sigma-Aldrich) were ACS reagent grade (>99.0% purity) unless otherwise noted. All solutions were prepared in water treated with the Barnstead Nanopure purification system (18.2 MΩ cm).

2.2. Micromodel Fabrication

[8] Standard photolithography techniques were used to fabricate all micromodels in silicon, as described by *Chomsurin and Werth* [2003] and *Willingham et al.* [2008]. The etched micromodel and pore structure are illustrated in Figure 1; the pore structure consists of a homogeneous array of cylinders arranged in a staggered pattern. Individual cylinders are 300 μm in diameter and spaced 180 μm apart in pore bodies and 40 μm apart in pore throats, resulting in a porosity of 0.39. The entire micromodel contains two inlet channels each with an inlet hole (A and B) drilled completely through the silicon using a 1.25 mm diameter diamond plated drill, a 2 cm × 1 cm area containing the pore network, and an effluent channel with an outlet drilled through the silicon wafer. The pore structure and inlet and outlet channels were etched to a depth of 35 μm. A 500 μm thick sheet of Pyrex glass was anodically bonded to the micromodel surface to create the flow channels. Nanoports (Upchurch Scientific) were attached to the back of the micromodel and held by adhesive. Teflon tubing (250 μm inside diameter) delivered fluid from two Milligat Flowpro pumps from solution reservoirs to each micromodel inlet via three-way PTFE (Polytetrafluoroethylene) valves.

2.3. Micromodel Experiments

[9] Precipitation experiments were performed using three different sets of inlet solutions listed in Table 1. Uranyl nitrate ($UO_2(NO_3)_2$, 100 μ*M*) and sodium phosphate dibasic (Na_2HPO_4, 100 μ*M*), were prepared in nanopure water. Calcium chloride ($CaCl_2$, 100 μ*M*) was dissolved in a 100 μ*M* $UO_2(NO_3)_2$ solution, and sodium sulfate (Na_2SO_4, 100 μ*M*) was dissolved in a 100 μ*M* Na_2HPO_4 solution to yield combined solutions. The concentration of U(VI) was chosen to represent those found at the Oak Ridge Field Research Center (84–210 μ*M*) [*Wu et al.*, 2006]; it exceeds maximum concentrations found at the Hanford site 300 area (4.2 μ*M*) [*Zachara et al.*, 2005] and the Fox Canyon site (23 μ*M*) [*USEPA*, 2000]. HPO_4^{2-}, Ca^{2+}, and SO_4^{2-} were added in a 1:1 molar ratio with U(VI). For comparison, Ca^{2+} concentrations include values from 0.25 to 4.2 m*M* at the Hanford site [*Moody et al.*, 1996; *Simon et al.*, 2008; *Zachara et al.*, 2005] and 2.5 to 41 m*M* at the Oak Ridge site [*USEPA*, 2000]. For SO_4^{2-}, concentrations include values from 0.25 to 0.61 m*M* at the Hanford site [*U.S. Department of Energy*, 1992; *Zachara et al.*, 2005; *Vermeul et al.*, 2007] and a value of 2.13 m*M* at the Oak Ridge site. Hence, experimental Ca^{2+} and SO_4^{2-} concentrations in this work are relatively low compared to the U.S. Department of Energy (DOE) sites. All inlet solutions were maintained in bottles open to the

Table 1. Experimental Matrix With Inlet Conditions

Experimental Name	Precipitation Conditions	
	Inlet A	Inlet B
UP	100 μ*M* $UO_2(NO_3)_2$, pH 4.5	100 μ*M* Na_2HPO_4, pH 6.7
UCaP	100 μ*M* $UO_2(NO_3)_2$, 100 μ*M* $CaCl_2$, pH 4.1	100 μ*M* Na_2HPO_4, pH 6.7
UPS	100 μ*M* $UO_2(NO_3)_2$, pH 4.5	100 μ*M* Na_2HPO_4, 100 μ*M* Na_2SO_4, pH 7.3

atmosphere at 31°C±1°C, and micromodels were kept at room temperature (21°C±0.5°C); the heated solutions were pumped through tubing that allowed the solutions to cool to 21°C before entering the micromodels. This approach ensured that dissolved gas concentrations were below saturation at 21°C and eliminated the evolution of gas bubbles in the micromodels. This approach also resulted in total dissolved carbonate concentrations (i.e., Tot(CO_3)) less than 0.11 m*M*, which are low compared to the values up to and exceeding 10 m*M* that can occur at some DOE sites such as Hanford and Rocky Flats [*Zachara et al.*, 2005; *Bostick et al.*, 2003]. The relatively low Ca^{2+} and Tot(CO_3) concentrations evaluated in this work allow a detailed analysis of uranium precipitation in the absence of other minerals. Higher Ca^{2+} and Tot(CO_3) concentrations are evaluated as part of our modeling effort to explore how these constituents may affect mineral precipitation.

[10] During precipitation experiments, inlet A was purged with $UO_2(NO_3)_2$ alone or in combination with $CaCl_2$. Inlet B was purged with Na_2HPO_4 alone or in combination with Na_2SO_4. Experiments with $UO_2(NO_3)_2$ and Na_2HPO_4 are referred to as UP; those with $CaCl_2$ added are referred to as UCaP; and those with Na_2SO_4 added are referred to as UPS (Table 1). Precipitation in each experiment was allowed to occur continuously for approximately 28 h. The volumetric flow rate was 75 μL h^{-1} through each syringe, corresponding to a Darcy velocity of 0.71 cm min^{-1} in the micromodel pore structure. This is similar to flow velocities observed in sands with high conductivities, such as at the 300 area Hanford site. In all images, fluid flow is from left to right, and the fluid residence time is approximately 65 s in the pore structure. All experiments were performed in duplicate.

2.4. Micromodel Visualization

[11] Experiments were imaged with a Nikon microscope (Eclipse Ti) equipped with 4X, 10X, and 40X inverted objectives, a digital camera (Photometrics Coolsnap HQ2), and an automated stage (Märzhäuser Wetzlar). The computer software NIS-Elements was used to control the microscope components and image acquisition. For example, the software was programmed to execute 26 × 3 stage movements and 78 image-capture events with the 10X objective (0.6 μm pixel resolution) at each time point and to montage the individual images into a complete image of the entire pore network. Using the same microscope, precipitates were analyzed through the glass cover slip using Raman backscattering spectroscopy for mineral identification. A laser of wavelength 532 nm was manually focused on an area with precipitate prior to each scan. The scattered light was collected by the focusing objective and passed through a Horiba Jobin Yvon LabRam-HR spectrometer with 1600 mm^{-1} gratings and captured by an air-cooled carbonate compensation depth. Collected spectra are an average of 10 or more exposures, each with a 10 s acquisition time. The Raman spectra were processed using the software program LabSpec. Precipitates were analyzed ex situ using a Rigaku μ-XRD system. X-rays were generated (MicroMax 007HF operated at 35 kV and 25 mA) from a rotating Cr target ($\lambda = 2.2910$ Å) and focused through a 300 μm diameter collimator. The X-ray beam cannot evaluate minerals through the glass cover slip, so the micromodel was cut across the outlet channel and the glass in this region with fixed mineral precipitates was broken free and mounted on the stage of a Rigaku D/Max Rapid II goniometer for analysis. Diffraction data recorded on a 2-D image plate were integrated between 10° and 160° 2θ to give powder traces. Exposure time for the samples was 10 min each. Comparison with database patterns (International Centre for Diffraction Data (ICDD), Pennsylvania) was carried out using JADE v9.2 (Materials Data Inc., California). The same sample was evaluated using a FEI Helios Nanolab dual-beam focused ion beam/SEM equipped with energy dispersive X-ray spectroscopy (EDXS). Samples were coated with carbon prior to analysis.

[12] Laser confocal imaging was used to determine whether mineral precipitates spanned the depth of the microfluidic pore structure and potentially blocked flow. The pore networks for UP, UCaP, and UPS experiments were filled with the fluorescein dye solution to provide contrast, and one upgradient pore and one downgradient pore were imaged using a Zeiss LSM710 multiphoton laser-scanning confocal microscope (Carl Zeiss MicroImaging, Inc.). Slices of 1 μm thick were acquired with a 488 nm Ar ion laser for excitation and detected at 500–570 nm with a 40X long working distance water immersion objective (approximately 1 μm resolution). They were montaged to obtain 3-D images of the precipitates.

[13] Tracer tests were conducted with a fluorescein dye (10 μ*M*) in order to determine whether mineral precipitates completely blocked pores. The dye was injected through inlet A at 100 μL h^{-1}, and nanopure water was injected through inlet B at 50 μL h^{-1}. When precipitates are not present, the fluorescent tracer occupies approximately two thirds of the pore structure. When precipitates block the pores, the fluorescent tracer is confined to the pore structure above the zone of precipitation along the centerline of the micromodel pore structure. The fluorescent dye was imaged using fluorescent microscopy and an ET-GFP (Green Fluorescent Protein) filter.

2.5. Image Analysis

[14] Mineral precipitates are darker (lower in intensity) than silicon etched flow channels containing water and silicon grains. Shadows extending 0–10 μm around each grain were also present and of similar intensity to mineral precipitates. A blank pore structure was created numerically, and grain sizes were adjusted to match grain plus shadow dimensions in the individual images; image subtraction was then used to eliminate silicon grains and shadows from further evaluation. Image thresholding of gray-scale intensity was used to distinguish mineral precipitates from etched flow channels containing water, and the number of pixels with precipitates was summed. Thresholding was performed over the unit region (480 μm × 480 μm) surrounding each cylinder using the *Otsu* [1979] method, which minimizes overlap of gray-scale intensity distributions for mineral precipitates and water, and then the threshold values obtained from the Otsu method were decreased by 0%–10% to correct for any remaining shadow effects (the intensity of the shadow was slightly higher than for precipitates). The estimated error in precipitation area from uniformly adjusting threshold values from the Otsu method over the entire image was smaller than 5%, compared to the cases with manually adjusted

threshold values from the Otsu method for each unit region. Total area was determined by multiplying the number of pixels by individual pixel area, and total volume was determined by assuming precipitates occupied the entire pore depth. It is unlikely that all precipitates spanned the entire pore depth, and observed gray-scale variations suggest packing density among mineral precipitates varied. Hence, estimated areas and volumes are semiquantitative and must be interpreted with caution.

[15] Precipitation rates were relatively constant over much of the experimental time and were approximated by linear regression of precipitate area versus time data from duplicate experiments. The areas of individual crystalline precipitates were determined in approximately five pores along the micromodel length in each unique precipitation experiment. The range of area values that individual crystalline precipitates occupied was determined based on the visual inspection of more than 40 crystals for each experiment. ImageJ [*Rasband*, 1997–2011] was used to count the area of each crystal, and an average area and standard deviation were determined.

[16] The transverse distance of continuous precipitates in the horizontal center of each pore was measured to determine if the precipitate width changed from pore to pore along the length of each micromodel. The edges of the continuous precipitate were selected manually, and the ImageJ [*Rasband*, 1997–2011] was used to measure the distance.

2.6. Pore-Scale Reactive Transport

[17] Pore-scale reactive transport was simulated to determine initial distributions of reactive solutes and saturation ratios (SRs) for each experimental system in the micromodel. Since only the initial distributions were simulated, the reactive transport model output was not used to calculate the amount of precipitation that occurred or to distribute precipitate in the micromodel pore structure. Fluid flow and reactive transport were solved in two dimensions because concentration gradients in the vertical dimension (i.e., with micromodel depth) are eliminated by fast diffusion over very short length scales [*Willingham et al.*, 2008]. The lattice-Boltzmann method (LBM) was used to solve fluid velocities in the pore space as described in our previous work [*Knutson et al.*, 2005]. Fixed pressure boundary conditions were imposed along the inlet ($x = 0$) and outlet ($x = L$), and the resulting steady flow field was scaled to the Darcy velocity used in the experiment. A finite volume method (FVM) was used for reactive transport and is an extension of the model we developed to simulate biofilm growth [*Knutson et al.*, 2005], bimolecular reactions [*Willingham et al.*, 2008, 2010], and heterogeneous reaction of calcium carbonate [*Yoon et al.*, 2012]. In this study, we assume homogeneous reactions are instantaneous, and the reactive transport equations in terms of the total concentration of the primary species (Ψ_j) in the liquid phase (Ω_p) are given by

$$\nabla \cdot (u\Psi_j - D\nabla\Psi_j) = 0 \qquad \text{in } \Omega_p, \tag{1}$$

$$\Psi_j = C_j + \sum_{i=1}^{N_{eq}} \upsilon_{ji} C_i, \tag{2}$$

where **u** is the steady velocity field from LBM, D is the diffusion coefficient, υ_{ji} are the stoichiometric coefficients, C_j and C_i are the solute concentrations of primary and secondary species in the liquid phase, respectively, and N_{eq} is the number of secondary species (subject to equilibrium reaction). In this study, the same diffusion coefficient for all species was used to avoid the violation of charge balance [*Lichtner*, 1985; *Liu et al.*, 2011]. Fixed concentrations and a zero gradient boundary condition were used at the inlet and outlet, respectively. The primary species (i.e., component species) in the model include UO_2^{2+}, $H_2PO_4^-$, Ca^{2+}, SO_4^{2-}, H^+, CO_3^{2-}, NO_3^-, and Na^+. The secondary species concentrations (C_i) are given through the mass action law as functions of the primary species concentrations,

$$C_i = \gamma_i^{-1} K_i \prod_{j=1}^{N_e} \left(\gamma_j C_j\right)^{\upsilon_{ji}}, \tag{3}$$

where γ_i is the activity coefficient, and K_i is the equilibrium constant. The activity coefficient is computed from the extended Debye-Hückel (D-H) equation. All constant values in the D-H equation are from *Helgeson and Kirkham* [1974] and *Helgeson et al.* [1981]. Once total concentrations of primary species are solved (equations (1) and (2)), equation (3) was solved simultaneously using the Newton-Raphson method. Accuracy of calculation was verified by comparing the speciation results for three different solutions in Table 1 over a range of pH values (4–9) with those calculated using MINEQL+ [*Schecher and McAvoy*, 1999] and Geochemist's Workbench [*Bethke and Yeakel*, 2009].

[18] The SR is defined as the ratio of ion activity product (Q) to the saturation product (K_{sp}) and is given by

$$\mathrm{SR} = \frac{Q}{K_{sp}} = \prod_{i=1} \frac{(\gamma_i C_i)^{\upsilon_i}}{K_{sp}}. \tag{4}$$

[19] An SR value less than one indicates that precipitation is not thermodynamically favorable. Aqueous reactions and stability constants used in this study are listed in Table A1. These were obtained from the EQ3/6 thermodynamic database [*Wolery*, 1992], the Nuclear Energy Agency database for uranium [*Bernhard et al.*, 2001; *Guillaumont and Mompean*, 2003], and *Dong and Brooks* [2006].

[20] We identified six uranium solid phases and HAP [$Ca_5(PO_4)_3(OH)$] as possible precipitates for the experimental conditions evaluated in this work. The six uranium solid phases are chernikovite, uranyl hydrogen phosphate (UHP), uranyl orthophosphate (UOP), Na-autunite, Ca-autunite, and metaschoepite. Two other less thermodynamically stable forms of calcium phosphate were initially evaluated because they may form in preference to HAP, i.e., amorphous calcium phosphate ($Ca_3(PO_4)_2 \cdot xH_2O$) and octacalcium phosphate ($Ca_4H(PO_4)_3 \cdot 2.5H_2O$) [*Van Kemenade and De Bruyn*, 1987; *Castro et al.*, 2012], but were not further considered because SRs for these solids were always much less than one under conditions considered in this work. The log K_{sp} values of these minerals were obtained from a recent review and updated experimental data [*Grenthe et al.*, 1992; *Gorman-Lewis et al.*, 2008a, 2008b, 2009; *Zhu et al.*, 2009]; they are listed in Table A2. In some cases, multiple K_{sp} values were available in the

Table 2. Total Concentration of Inlet Reactants Used in Simulations

Total Concentration[a]	UP Experiment (Measured)		UP Experiment (Calculated)[a]		UCaP Experiment (Measured)		UCaP Experiment (Calculated)[a]		UCaP High Ca^{2+} Case		UCaP High Tot(CO_3) Case		UPS Experiment (Measured)		UPS Experiment (Calculated)[a]	
	Inlet A[b]	Inlet B[c]	Inlet A[b]	Inlet B[c]	Inlet A[b]	Inlet B[c]	Inlet A[b]	Inlet B[c]	Inlet A[b]	Inlet B[c]	Inlet A[b]	Inlet B[c]	Inlet A[b]	Inlet B[c]	Inlet A[b]	Inlet B[c]
Tot(UO_2)	1.00E-4		1.00 E-4		1.00 E-4		1.00 E-4		1.00 E-4		1.00 E-4		1.00 E-4		1.00 E-4	
Tot(H)	2.00 E-5	1.13 E-4	1.63 E-4	2.67 E-5	8.00 E-5	1.13 E-4	1.63 E-4	2.67 E-5	8.00 E-5	1.13 E-4	7.50 E-3	5.00 E-3	2.00 E-5	1.00 E-5	1.63 E-4	2.64 E-5
Tot(H_2PO_4)		1.00 E-4		1.00 E-4		1.00 E-4		1.00 E-4		1.00 E-4		1.00 E-4		1.00 E-4		1.00 E-4
Tot(CO_3)	1.02 E-5	1.06 E-4	1.02 E-5	6.32 E-5	1.02 E-5	1.06 E-4	1.02 E-5	6.32 E-5	1.02 E-5	1.06 E-4	5.00 E-3	5.00 E-3	1.02 E-5	6.30 E-5	1.02 E-5	6.30 E-5
Tot(Na)		2.00 E-4		2.00 E-4		2.00 E-4		2.00 E-4		2.00 E-4		2.00 E-4		4.00 E-4		4.00 E-4
Tot(NO_3)	2.00 E-4		2.00 E-4		2.00 E-4		2.00 E-4		2.00 E-4		2.00 E-4		2.00 E-4		2.00 E-4	
Tot(Ca)					1.00 E-4		1.00 E-4		1.00 E-2		1.00 E-4					
Tot(SO_4)														1.00 E-4		1.00 E-4
pH (31°C)	4.45	6.7	3.83	7.1	4.13	6.7	3.83	7.10	4.14	6.71	6.22	7.93	4.45	7.3	3.83	7.1

[a]Total concentrations of the primary species were computed using equation (2), and aqueous speciation reactions are listed in Table A1. Units are in the molar concentration (*M*).
[b]Inlet A contains $UO_2(NO_3)_2$ in all experiments, in addition to $CaCl_2$ in the UCaP experiment.
[c]Inlet B contains Na_2HPO_4 in all experiments, plus Na_2SO_4 in the UPS experiment.

literature; either the most recent, the medium, or a range was considered. For example, log K_{sp} values for chernikovite varied from −22.73 [*Van Haverbeke et al.*, 1996] to −25.1 [*Johnson*, 2000]; a log K_{sp} value of −24.2 was used because it was recommended by *Grenthe et al.* [1992] and recently used by *Guillaumont and Mompean* [2003]. The log K_{sp} value of −25.1 was also evaluated to determine maximum SRs for this mineral. The log K_{sp} values for UHP, UOP, and Ca-autunite were reported as mean values (−25.52, −49.36, and −48.36, respectively), plus or minus two standard deviations from reported experimental data [*Gorman-Lewis et al.*, 2009]. The mean and standard deviation values were used in this work. Single values of log K_{sp} were used for Na-autunite and metaschoepite; they are from the literature and were used without consideration of errors. For HAP, two log K_{sp} values obtained from the synthetic HAP dissolution experiments were used (−53.28 from *Zhu et al.* [2009] and −58.0 from *Valsami-Jones et al.* [1998]).

2.7. Model Application Scenarios

[21] Simulations were performed in the first three pore bodies to reduce computational time. SRs are highest at this location because concentrations are highest near the inlets; this provides the maximum initial SRs and allows for direct comparison to minerals that precipitated in micromodel experiments. A uniform grid spacing of 5 μm is used for both the LBM and FVM, which results in 60 grid cells across a grain and 7 grid cells across a pore throat. A grid spacing of 5 μm was previously used to simulate different biochemical reactions in an identical pore structure with adequate accuracy [*Knutson et al.*, 2005; *Willingham et al.*, 2008, 2010; *Yoon et al.*, 2012]. Inlet conditions evaluated by the model are listed in Table 2. These include the experimental conditions and two additional conditions that consider either a higher concentration of Ca^{2+} (10 m*M*) or a higher concentration of Tot(CO_3) (5 m*M*) compared to the experimental UCaP conditions (i.e., Tot(Ca) = 0.1 m*M* and Tot(CO_3) = 10^{-2} m*M*). These two additional cases were simulated to evaluate thermodynamic favorability of mineral precipitation under Ca^{2+} and total carbonate concentrations more representative of DOE field sites as described previously. Inlet concentrations of total primary species are computed based upon both measured and calculated pH values of inlet solutions. Calculated values were determined from inlet solution concentrations in Table 1 and carbonate species concentrations based on equilibration of influent solutions with atmospheric CO_2 at 31°C. Differences in measured and calculated values are likely due to insufficient equilibration of influent solutions with the atmosphere and small errors in pH measurement. We will show that these differences only marginally affect calculated SR values. The diffusion coefficients for all aqueous species are assumed to be equal and were set to 1.0×10^{-5} cm^2 s^{-1} as a reference value. *Yoon et al.* [2012] demonstrated that the diffusion coefficient can affect mineral precipitation rates. Consequently, two additional *D* values of 0.3×10^{-5} and 2×10^{-5} cm^2 s^{-1} were evaluated; this represents the upper and lower bounds of *D* values for elements of interest in radionuclide transport [*Lerman*, 1979].

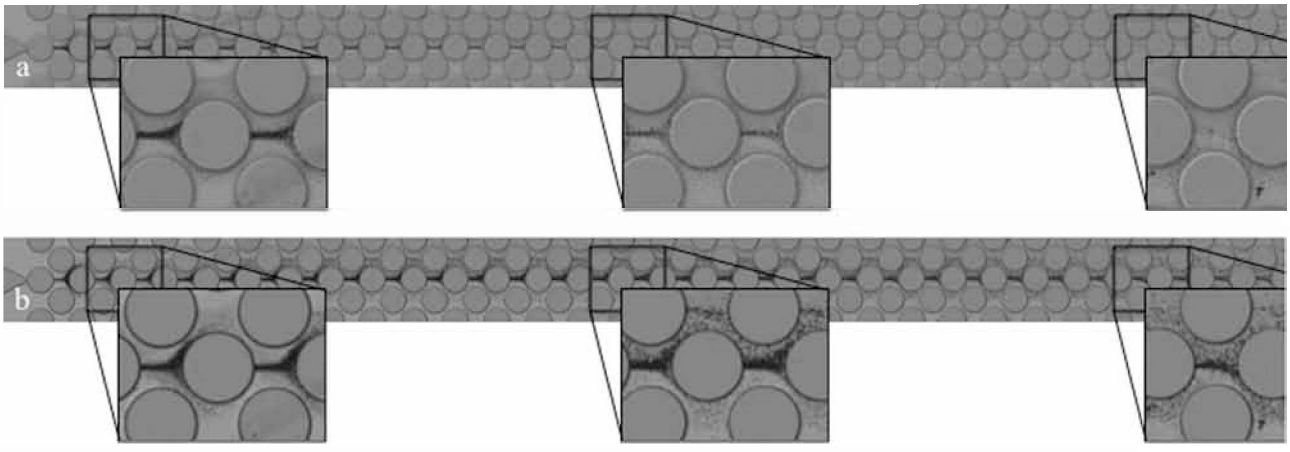

Figure 2. Brightfield reflected microscopy images (10X objective) of precipitate in the UP system after (a) 7.5 h and (b) 27.5 h.

3. Results and Discussion

3.1. Precipitate Morphology

[22] Brightfield reflected microscopy images for one of the UP experiments at two time points during precipitation are shown in Figure 2. Uranium and phosphate mixed along the horizontal center region of the micromodel pore structure due to diffusive mixing and precipitated in this region. Minerals formed first on the influent side of the micromodel pore network and later over the entire length of the pore network. Minerals formed more quickly upgradient because reactant concentrations were greater (i.e., greater SRs); diffusive mixing downgradient diluted the concentrations, making precipitate formation slower [*Zhang et al.*, 2010]. Upgradient at early time (7.5 h), and along the entire length of the micromodel at late time (27.5 h), precipitates appear as dense agglomerations of small crystals in the center of pore bodies. Less precipitation occurs in pores directly adjacent to the middle pore due to diffusion-limited mixing across the horizontal centerline. The same behavior was observed for mineral precipitates in the UCaP and UPS experiments (not shown).

[23] High-resolution brightfield microscopy images of crystalline precipitates in individual pores of the UP, UCaP, and UPS experiments are shown at similar times in Figure 3. A thick zone of agglomerated crystals is present along the horizontal center of each pore for UP and UCaP. Away from the thick precipitate zones, and throughout the pore for UPS, individual crystals are present. These appear smaller for UP and UCaP compared to UPS and more amorphous for UCaP compared to UP and UPS. At least 40 individual crystal sizes were determined in at least five pores along the horizontal center zone of each micromodel experiment. Individual crystal sizes in the UP, UCaP, and UPS systems are 54 ± 37, 72 ± 45, and 170 ± 101 μm^2, respectively; a plot of cumulative frequency distributions for individual crystal areas are in Figure A1. Average values increase from UP, to UCaP, to UPS, and the wide distribution of crystal sizes in each experiment results in significant overlap. The combination of crystal size results and images suggests, as hypothesized, that the presence of Ca^{2+} and SO_4^{2-} affects crystal size and morphology.

3.2. Precipitation Rates

[24] Amounts of precipitate over time in the UP, UCaP, and UPS experiments are shown in Figure 4. Fluid residence time in the micromodel is approximately 1.1 min.

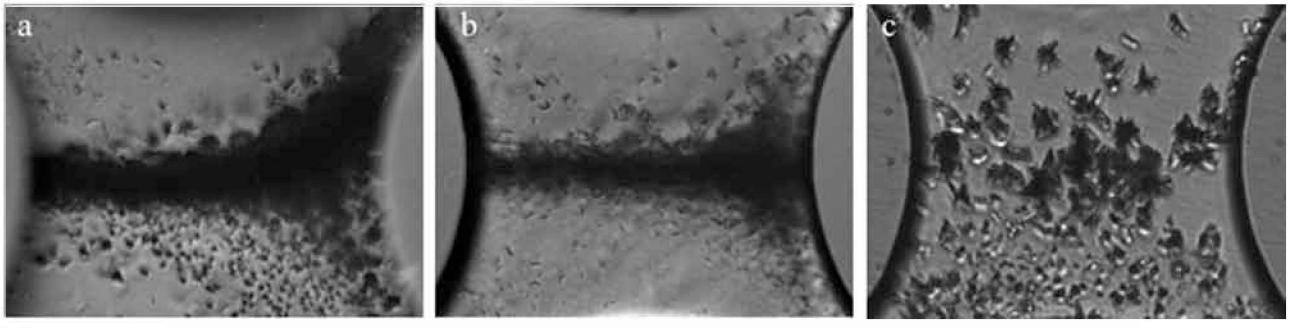

Figure 3. High-resolution (40X objective) brightfield microscopy images showing crystal sizes in single pores of the (a) UP, (b) UCaP, and (c) UPS systems. The pores are located near the inlet, and images were taken after approximately 12–15 h. Individual images are 200 μm in width.

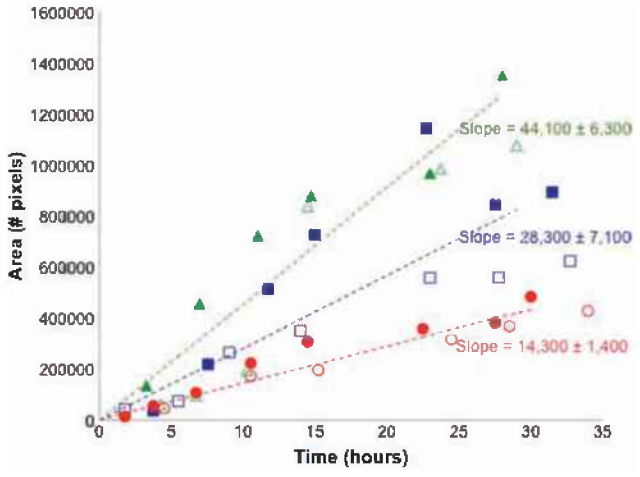

Figure 4. Area containing mineral precipitates versus time for the three replicate experiments. Slopes are shown and represent mineral precipitation rates. UP (rectangles), UCaP (triangles), and UPS (circles) are shown.

The reactants diffuse across the center mixing line and reach steady-state conditions relatively quickly with concentration gradients in the horizontal plane of the experiment. Hence, the concentration profiles in the micromodel are relatively constant in time and only change slowly as precipitates block pores. As a result, reactions that occur are limited by the kinetics of chemical reaction. For much of the precipitation period, the area with precipitates increases linearly with time. However, at late time some deviation is evident for UP and UCaP, as the amount of precipitate starts to level off as steady state is approached. Assuming a constant rate of precipitation, linear regression yields precipitation rates of 28,300±7100 pixels h^{-1} for UP, 44,100±6300 pixels h^{-1} for UCaP, and 14,300±1400 pixels h^{-1} for UPS. Results presented here support our hypothesis that the presence of Ca^{2+} and SO_4^{2-} affect uranium precipitation rates; they also demonstrate that Ca^{2+} enhances the kinetics of uranium precipitation, while SO_4^{2-} inhibits it for the conditions tested.

3.3. Mineral Type and Composition

[25] Representative backscattering Raman spectra for the UP, UCaP, and UPS systems during precipitation are shown in Figure 5. All the three spectra are very similar and match the published spectrum for chernikovite, shown in the inset of Figure 5 [*Dorhout et al.*, 1989]. The exceptions are two broad peaks at 515 and 1350 cm^{-1} and an intense, sharp peak at 521 cm^{-1}, which arises from the silicon component of the micromodel [*Zhang et al.*, 2010]. The broad peaks are present in all experiments and are associated with chernikovite Raman spectra and may represent a less crystalline component of this mineral [*Zhang et al.*, 2010]. The peaks at 192 and 830 cm^{-1} are assigned to the UO_2 symmetric bending and stretching modes, respectively, whereas the peak at 1000 cm^{-1} is assigned to the PO_4 symmetric stretch [*Dorhout et al.*, 1989]. We note that the molecular formula for UHP differs from chernikovite by a single water molecule, and no Raman reference spectrum is available for UHP. Hence, while the Raman results do not rule out precipitation of UHP, they do suggest formation of chernikovite. The μ-XRD results for mineral precipitates formed in the UPS experiments and a reference chernikovite pattern (diffractogram) are shown in Figure 6. The patterns are very similar, indicating that only chernikovite is present. The experimental pattern contains some additional weak and shoulder peaks that are not present in the reference pattern; however, all these additional peaks are predicted in a diffraction pattern calculated from the crystal structure [*Morosin*, 1978]. The μ-XRD pattern for UCaP (not shown) also matches the chernikovite reference, indicating that this is the only mineral present in all the three experiments. We note that XRD reference patterns are available for a range of uranium phosphate compositions, and none of these, with the exception of chernikovite, match the experimental data satisfactorily. This includes phases which in place of the 4 waters of crystallization in chernikovite had 2 (ICDD pattern 13-0061), 1 (33-1428), and 1.7 (47-0176) waters of crystallization. Hence, it appears that only chernikovite is present in all the three experiments, in contrast to our hypothesis that the presence of Ca^{2+} and SO_4^{2-} affects the type of mineral precipitate.

[26] Since the presence of Ca^{2+} and/or SO_4^{2-} affected the rate of mineral precipitation, crystal size, and crystal morphology, but only chernikovite was detected in all the three experiments, EDXS was used to determine if Ca or S substituted into the chernikovite crystal structure. A typical EDXS spectra for UCaP and three corresponding ESEM (Environmental Scanning Electron Microscope) images are shown in Figure 7. The EDXS spectrum shows that only U, P, O, Si, Na, and C are present, not Ca. The Si peak is from the glass coverslip that is fixed to the mineral precipitate.

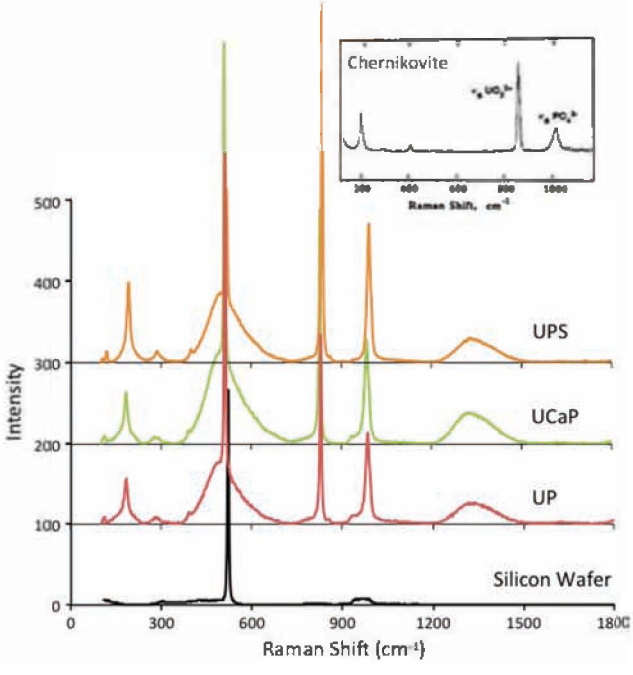

Figure 5. Raman spectra for the (top) UPS, (middle) UCaP, and (bottom) UP systems. Inset: Raman reference spectra for chernikovite from *Dorhout et al.* [1989].

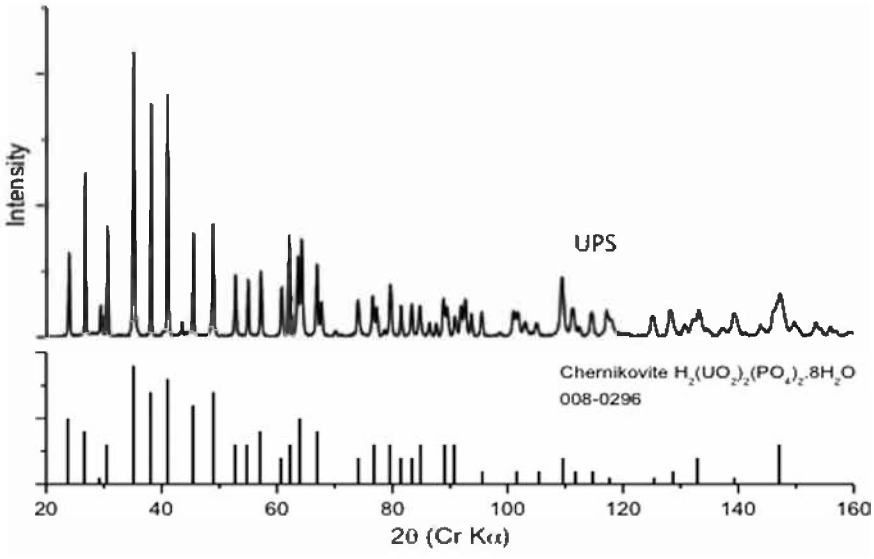

Figure 6. (top) μ-XRD pattern for mineral form in the UPS system and (bottom) comparison to reference pattern for chernikovite.

The Na peak is very small and is likely due to Na^+ adsorption onto the chernikovite surface. The C is carbon coating. Peak heights for other EDXS spectra of UCaP vary slightly but always show the same elements. EDXS results for UPS are similar (results not shown); U, P, O, Si, Na, and C were identified, but no S was detected. Hence, Ca and S do not appear to substitute into the chernikovite crystal structure. The corresponding ESEM images for UCaP (Figure 7) illustrate the complex morphology of chernikovite; it is comprised of thin plates stacked together in a dense framework or of thin plates connected at irregular angles in an open framework. *Dunham–Cheatham et al.* [2011] observed thin plates of uranyl phosphate precipitates under conditions similar to UP. The effects of Ca^{2+} and SO_4^{2-} on uranium precipitation rates will be discussed later.

3.4. Model Results

[27] The distribution of dominant soluble uranium species and pH without consideration of precipitation reactions are shown in Figure 8 based on the experimental measurements of pH. The dominant uranium species are UO_2^{2+}, UO_2OH^-, UO_2HPO_4, and $(UO_2)_2(CO_3)(OH)_3^-$. All but $(UO_2)_2(CO_3)(OH)_3^-$ are primarily present below the horizontal centerline of the pore structure where the uranium concentration is higher. For all the three systems, UO_2^{2+} has much higher concentrations than any other uranyl complexes below the horizontal centerline where the pH is lower (pH<6). At the low pH, anion (OH^-, CO_3^{2-}, HPO_4^{2-}) concentrations to form uranyl complexes are very low, resulting in low concentrations of uranyl complexes compared to UO_2^{2+}. The $(UO_2)_2(CO_3)(OH)_3^-$ is primarily present above the centerline of the micromodel where the pH and therefore CO_3^{2-} are higher. The maximum concentrations of each soluble uranium species are within a factor of two (and often identical) for UP and UPS. These concentrations are within a factor of four (and often within a factor of two) compared to UCaP. For UCaP (compared to UP and UPS), the maximum concentration of UO_2^{2-} is higher, and the maximum concentrations of UO_2OH^- and $(UO_2)_2(CO_3)(OH)_3^-$ are lower because of the lower measured pH value. If the calculated pH values are used (i.e., those based on equilibration with atmospheric CO_2 at 31°C), then concentrations of UO_2^{2+}, UO_2OH^-, UO_2HPO_4, or $(UO_2)_2(CO_3)(OH)_3^-$ would be almost identical in each experiment because aqueous uranium species concentrations with sulfate and calcium are relatively low.

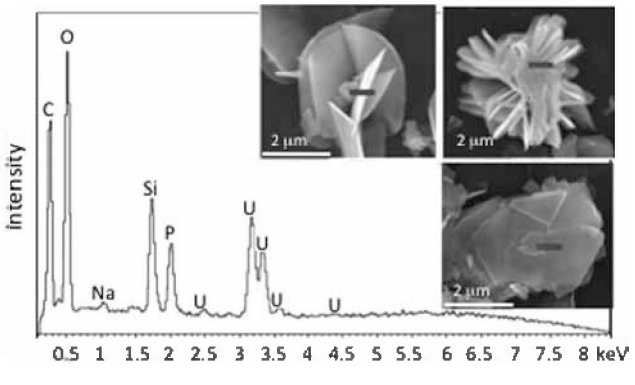

Figure 7. EDXS spectrum for UCaP, with three inset SEM images of crystalline precipitates.

[28] The distribution of SR values that correspond to the experimental conditions simulated in Figure 8 is computed to compare experimental results with thermodynamic predictions as shown in Figure 9. Maximum SR values are located near the horizontal centerline of the pore structures, where the reactants mix. Maximum SR values for the experimental conditions simulated in Figure 9 are listed in Table 3. Also listed are maximum SR values when calculated pH values are used, and maximum SR values when the range of K_{sp} values and diffusion coefficients in the

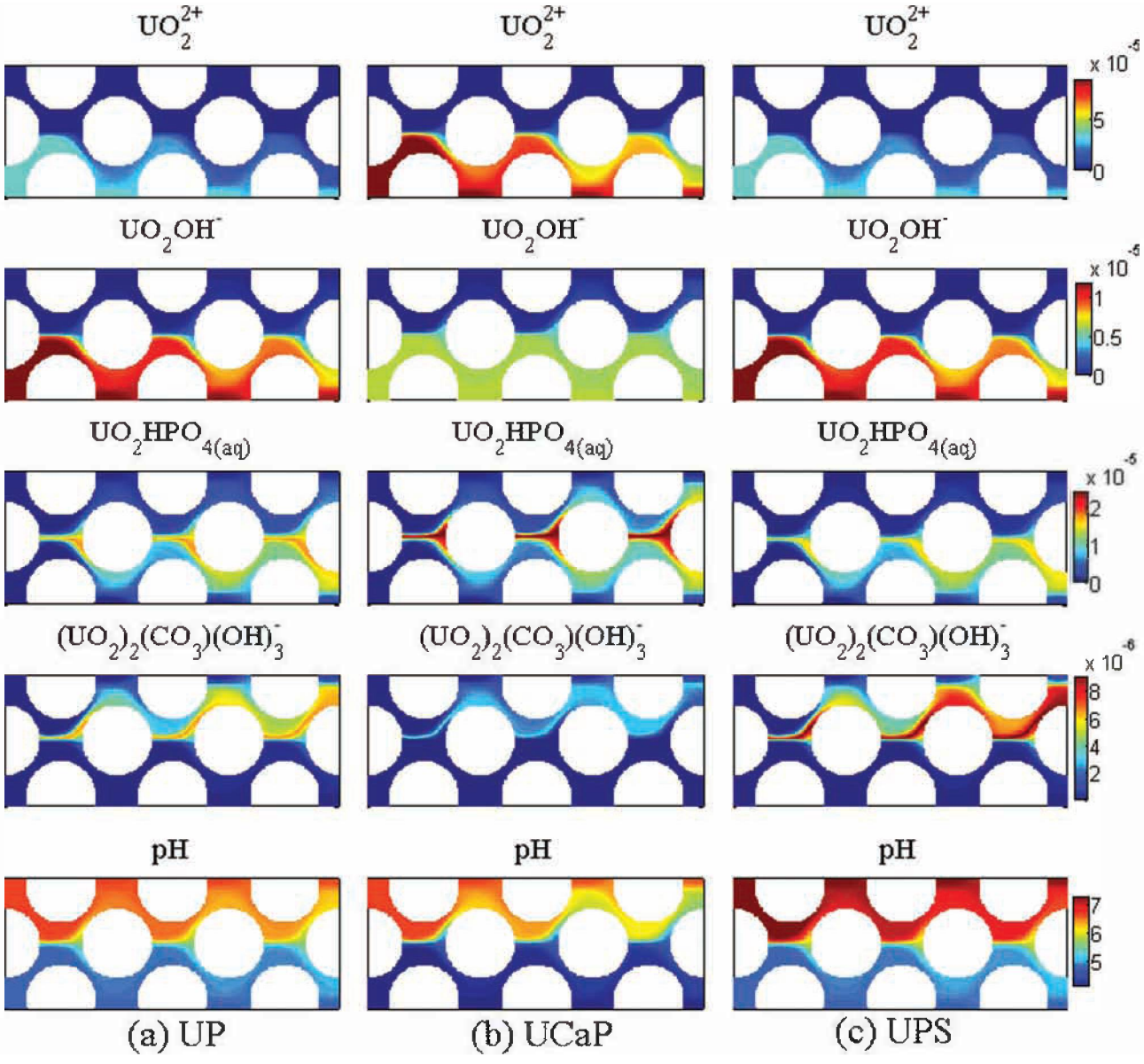

Figure 8. Calculated distribution of dominant soluble U(VI) species including the uncomplexed uranyl ion, uranyl hydroxide, uranyl phosphate, uranyl carbonate complexes, and pH for (a) UP, (b) UCaP, and (c) UPS. For all cases, the experimental conditions (not the calculated conditions) in Table 2 were considered.

literature are considered. Use of either set of pH values results in only very small changes in maximum SR values, so those based on experimental pH values are discussed hereafter. Based on the range of available literature values for K_{sp} used in this work, maximum SR values for chernikovite change by an order of magnitude but change by less than 50% for other minerals (and often much less). Hence, different SR values will only be discussed for chernikovite. Use of different diffusion coefficients does not change the maximum SR values (Table 3), but the mixing zone width does change in proportion to the magnitude of the diffusion coefficient. Since our modeling focus is on the maximum SR values, and not the precipitation kinetics, only results with the reference diffusion coefficient value (i.e., 10^{-5} $cm^2\ s^{-1}$) are discussed further.

[29] The maximum SR values of experimental simulations reported in Table 3 for chernikovite, UHP, and Na-autunite are all less than 40, whereas those for UOP are greater than 10^5. Maximum SR values for chernikovite, UHP, or UOP are not significantly different in all the three experiments. Maximum SR values for Na-autunite vary by a factor of approximately two between different experiments; this range of variation is small relative to differences in the maximum SR values for different minerals. When Ca^{2+} is present at 0.1 m*M*, the maximum SR value for Ca-autunite is greater than 10^6. Hence, UOP and

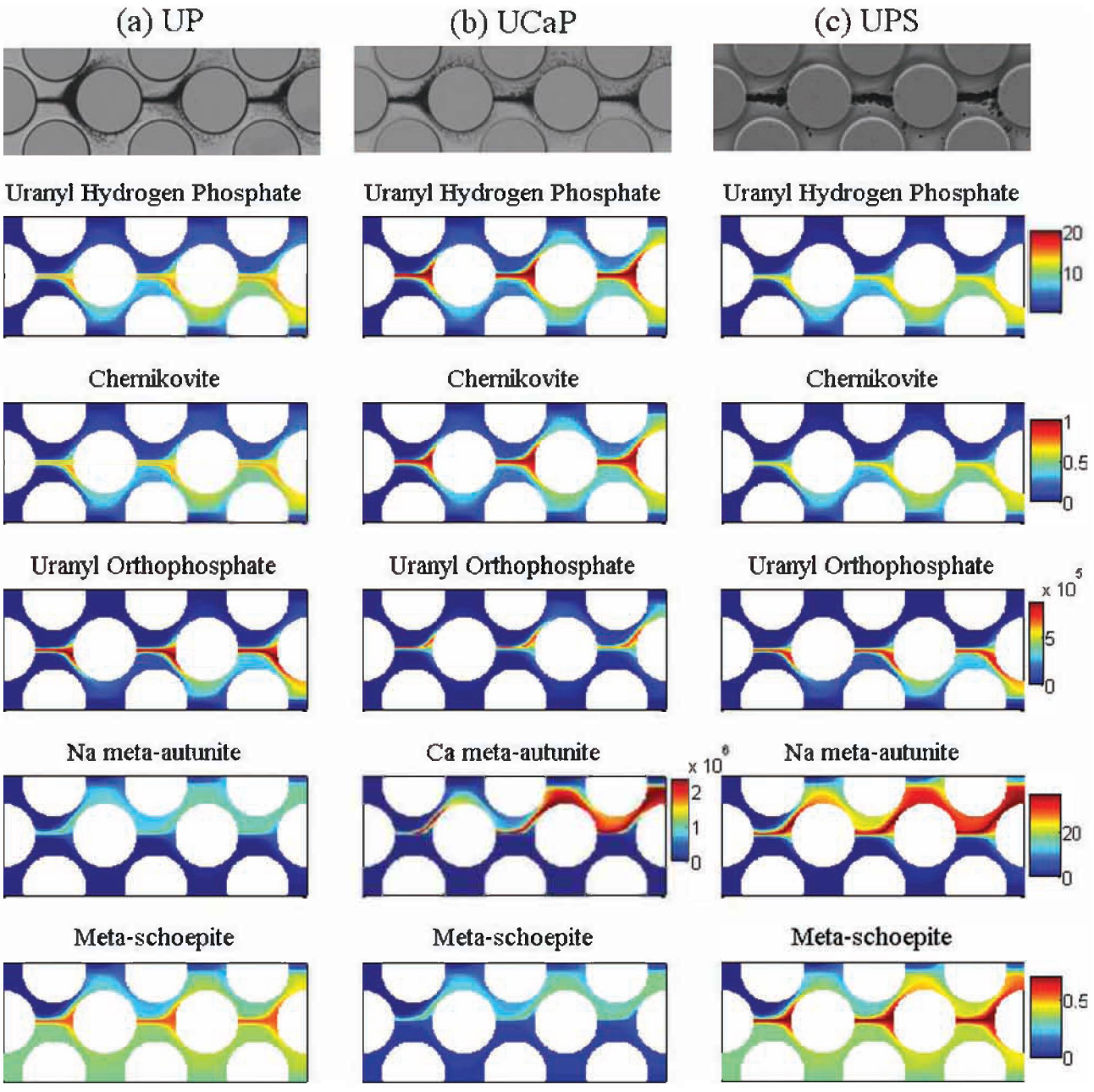

Figure 9. Distribution of SRs of six different U(VI)-phosphate minerals for (a) UP, (b) UCaP, and (c) UPS. For all cases experimental conditions in Table 2 were considered.

Ca-autunite are much more thermodynamically favored to precipitate. The ranges of the maximum SR values for UHP and Na-autunite are 13–21 and 14–37, respectively. The ranges of the maximum SR values for metaschoepite and HAP are 0.5–0.7 and $<10^{-5}$, respectively. Thermodynamic favorability of mineral precipitation depends on the solubility product (K_{sp}). For chernikovite, the maximum SR values are all less than 1 when the recommended literature value of K_{sp} is used, and between 8 and 14 when the lowest K_{sp} [*Johnson*, 2000] available is used. These results indicate that chernikovite is among the least thermodynamically favored mineral to precipitate in the micromodel experiments, even though it is the only one identified with Raman spectroscopy and μ-XRD spectroscopy.

[30] The maximum SR values for the two additional simulations performed with elevated Ca^{2+} (i.e., 10 m*M*) or total carbonate (i.e., 5 m*M*) are also listed in Table 3. For $[Ca^{2+}] = 10$ m*M*, there is no change in the relative favorability of minerals that will precipitate, although maximum SR values for HAP and Ca-autunite increased from $<10^{-5}$ to 0.004 and 2.24×10^6 to 1.95×10^8, respectively, due to the higher Ca^{2+} concentration. For $Tot[CO_3] = 5$ m*M*, there is also no change in the relative favorability of minerals that will precipitate, although the maximum SR values for chernikovite and UHP dramatically decrease to 0.0076

Table 3. Maximum SR

	Chernikovite		UHP	UOP	Na-Autunite	Ca-Autunite	Metaschoepite
	SR[a]	SR[b]	SR ($-2\sigma/+2\sigma$)[c]	SR ($-2\sigma/+2\sigma$)[c]	SR	SR ($-2\sigma/+2\sigma$)[c]	SR
UP_exp (meas)[d]	0.70 (0.70)	9.61	14.54 (12.38/18.73)	8.54E+5 (8.16E+5/9.36E+5)	16.28		0.56
UP_exp (calc)[e]	0.89 (0.89)	12.27	18.58 (15.81/23.94)	4.30E+5 (4.11E+5/4.71E+5)	16.76		0.35
UCaP_exp (meas)[f]	0.97 (0.97)	13.39	20.26 (17.25/26.10)	6.77E+5 (6.47E+5/7.42E+5)	14.79	2.33E+6 (2.17E+6/2.50E+6)	0.26
UCaP_exp (calc)	0.89 (0.89)	12.27	18.57 (15.81/23.93)	4.30E+5 (4.11E+5/4.71E+5)	16.75	2.24E+6 (2.09E+6/2.40E+6)	0.34
UCaP_high Ca^{2+} case	0.93	12.82	19.50 (16.60/25.13)	6.40E+5 (6.12E+5/7.01E+5)	13.67	1.95E+8 (1.82E+6/2.09E+6)	0.33
UCaP_high Tot(CO_3) case	0.0076	0.10	0.16 (0.14/0.21)	1.52E+1 (1.45E+1/1.66E+1)	0.58	2.24E+4 (2.09E+4/2.40E+4)	0.10
UPS_exp (meas)	0.64 (0.64)	8.80	13.32 (11.33/17.15)	7.82E+5 (7.46E+5/8.57E+5)	37.01		0.72
UPS_exp (calc)	0.88 (0.88)	12.12	18.34 (15.61/23.63)	4.25E+5 (4.05E+5/4.66E+5)	33.27		0.35

[a]SR is based on the K_{sp} value from *Grenthe et al.* [1992]. Maximum SR values in parentheses were obtained with lower (0.3×10^{-5} cm^2 s^{-1}) and upper (2.0×10^{-5} cm^2 s^{-1}) molecular diffusion coefficients, while a reference value (1×10^{-5} cm^2 s^{-1}) of diffusion coefficient was used for all other cases.
[b]SR is based on the K_{sp} value from *Johnson* [2000].
[c]SR values are based on the mean and standard deviation of K_{sp} values from *Gorman-Lewis et al.* [2009]. σ is the standard deviation of each SR.
[d]Exp: measured pH value was used to calculate pCO_2, and speciation equations in Table A1 were used to obtain initial distribution of species.
[e]Calc: pH and total carbonate concentration are calculated based on speciation reported in Appendix A. pCO_2 is assumed in equilibrium with atmosphere ($pCO_2=10^{-3.5}$).
[f]For UCaP experimental system, the maximum SR for HAP was less than 1. E-5 with a K_{sp} value of −58.0 from *Valsami-Jones et al.* [1998].

and 0.16, compared to experimental values of 0.97 and 20.3, respectively. Also, the maximum SR value for Ca-autunite decreased by two orders of magnitude to 2.24×10^4. The lower SR values for chernikovite, UHP, and Ca-autunite are mainly due to the formation of uranyl carbonate complexes in solution (i.e., $UO_2CO_{3(aq)}$, $(UO_2)_2CO_3(OH)_3^-$, $Ca_2UO_2(CO_3)_3$). Hence, for Ca^{2+} and Tot(CO_3) concentrations more representative of actual field sites, chernikovite is still among the least thermodynamically favored mineral to precipitate, and HAP precipitates, which can sequester uranium [*Wellman et al.*, 2008], also remain unfavorable. We note that for higher Ca^{2+} and PO_4^{3-} concentrations (i.e., 1 m*M* each) and higher pH (i.e., 9.8) (results not shown), HAP precipitation will be favorable and can represent a sink for uranium removal by sorption.

[31] Precipitates of chernikovite were recently observed by XRD, SEM (or transmission electron microscope), and/or EXAFS (Extended X-ray adsorption fine structure) in batch studies under uranium and phosphate concentrations similar to those used in the UP system of this study [*Singh et al.*, 2010; *Dunham-Cheatham et al.*, 2011]. In those studies, thermodynamically more favorable solid forms other than chernikovite were not observed as in this study. These results suggest that the formation of UOP is not kinetically favorable during experimental periods in this study. At room temperature, meta-autunite minerals such as Ca-autunite and Na-autunite have been synthesized by ion exchange of Ca or Na with the hydrogen ion in chernikovite, and reaction times on the order of a few days or less are indicated [*Sowder et al.*, 2001; *Wellman et al.*, 2005]. However, very high concentrations of cations (approximately 2 *M*) were used to obtain the more crystalline autunite. As described earlier, the EDXS spectrum for precipitates in our work shows no Ca and only very small peaks of Na. This suggests that under low Na^+ or Ca^{2+} concentrations, ion exchange of the proton in chernikovite did not occur or was not stable during precipitation (<30 h). *Jerden and Sinha* [2003] also stated that the formation of the autunite group minerals takes 2–3 weeks at room temperature. *Singh et al.* [2010] also observed metastability of chernikovite formed within a day over a 1 year experimental period in a batch system. Longer-term experiments are needed to assess if autunite is formed over longer time periods and in the presence of higher Na^+ or Ca^{2+} concentrations.

3.5. Effects of Ca^{2+} and SO_4^{2-} on Uranium Precipitation

[32] Several additional studies have investigated the impact of Ca^{2+} on uranium transformation at room temperature. *Sowder et al.* [1996] found that at 25°C, schoepite was slowly transformed to Ca-autunite for 94 days after schoepite was in a solution with 10 m*M* Ca^{2+} and PO_4^{3-}. Later, *Sowder* [1998] reported that Ca-autunite was synthesized from chernikovite in a high concentration Ca^{2+} solution (>0.01 *M*) by ion exchange at 22°C. Another study investigated the impact of Ca^{2+} on U(VI) sorption and found that the presence of Ca^{2+} reduced the sorption of U(VI) onto quartz [*Nair and Merkel*, 2011]. While these and aforementioned experiments indicate that Ca^{2+} in solution can promote the transformation of uranium from one mineral form to another or inhibit uranium sorption from solution, they do not provide insights into the effects of Ca^{2+} on uranium

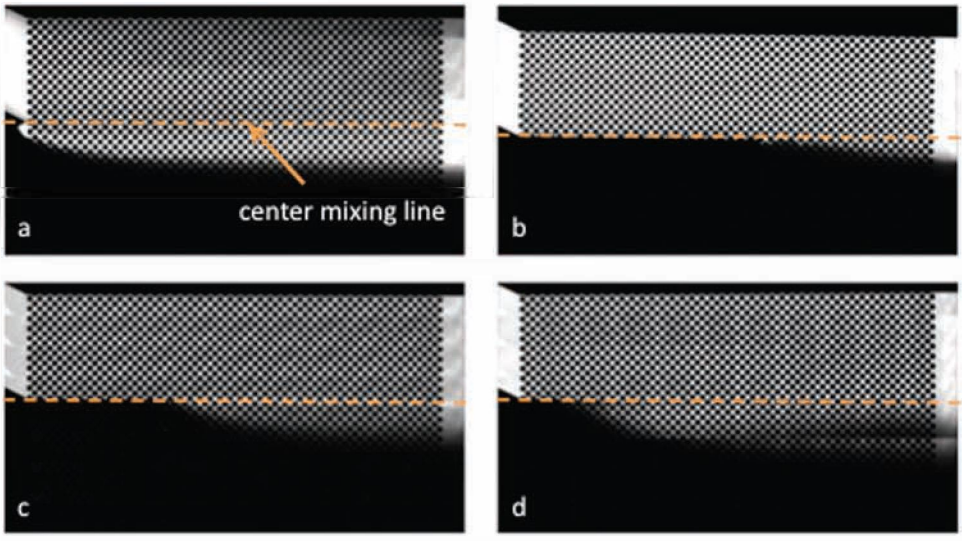

Figure 10. Tracer test results for (a) blank micromodel, (b) UP, (c) UCaP, and (d) UPS systems.

precipitation rates. Instead, our modeling results can provide insights. When Ca^{2+} is present (i.e., UCaP), maximum SR values for both chernikovite and UHP are greater compared to the UP case. These results suggest that the higher precipitate rate for UCaP compared to UP may be related to greater values of SR for chernikovite and/or UHP.

[33] Although we could find no supporting studies on the effects of SO_4^{2-} on uranium precipitation rates, there is extensive work regarding the effects of ions on calcium phosphate precipitation. In batch experiments under pH static conditions, *Cao et al.* [2007] observed that SO_4^{2-} reduced the rate of hydroxyapatite precipitation under supersaturated conditions. Aqueous SO_4^{2-} concentrations decreased at early time (within 10 min) during precipitation and then increased within an hour to the end of experiment (24 h). As a result, the final SO_4^{2-} concentration in the batch experiment was similar to the starting concentration, but the HAP precipitation rate was lower compared to that in a control experiment without SO_4^{2-}. The radius of SO_4^{2-} is smaller than that of phosphate; the authors proposed that the replacement of SO_4^{2-} into the HAP lattice at early stage decreased precipitation rates, but this replacement was not stable such that PO_4^{3-} replaced SO_4^{2-} in the lattice over time. We propose that a similar mechanism may be occurring in chernikovite for UPS.

3.6. Potential Pore Blockage Due to Precipitation

[34] Tracer test results for a clean micromodel and for the UP, UCaP, and UPS experiments after precipitation are shown in Figure 10. In the blank micromodel (i.e., no precipitate present), the tracer occupies two thirds of the pore structure, consistent with the 2:1 ratio of tracer to clean water flow rate. In micromodels with precipitate, the tracer is restricted to half of the micromodel for part of the pore structure, and then breakthrough across the precipitate zone occurs. This breakthrough occurs earliest in the pore structure for UPS, later in the pore structure for UCaP, and latest in the pore structure for UP. The maximum transverse widths of continuous precipitate as a function of longitudinal distance in the pore networks of the three experiments

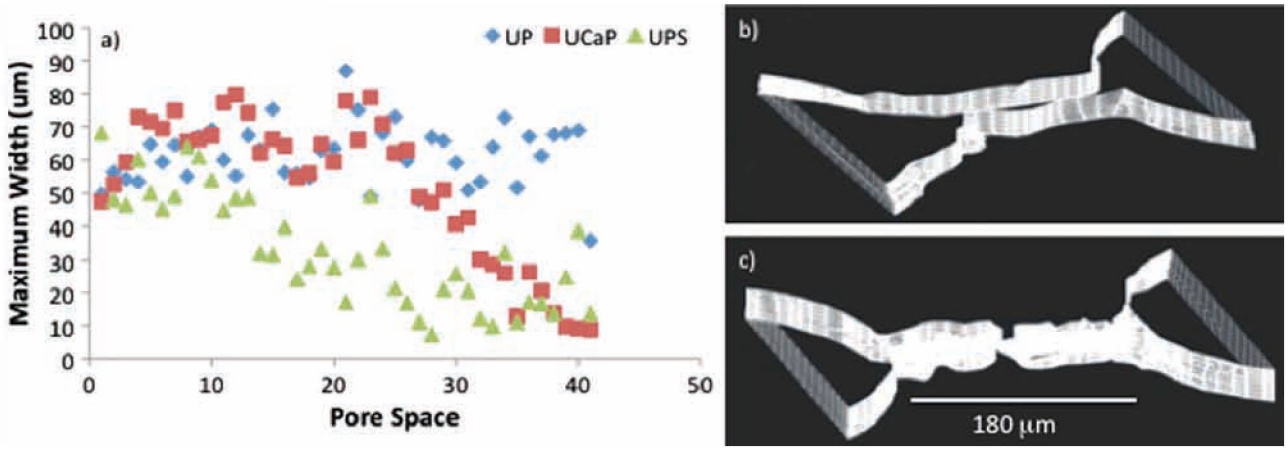

Figure 11. (a) Maximum transverse width of the precipitate line versus distance in the micromodel. (b and c) Montages of laser confocal images of mineral precipitates in individual pores from the (b) UP and (c) UPS systems halfway down the length of the micromodel.

are shown in Figure 11, along with laser confocal images of precipitate in a pore halfway down the length of the micromodel in the UP and UPS experiments. The transverse width is relatively constant over the entire pore length for UP but decreases midway in the pore network for UCaP and earlier in the pore network for UPS. Laser confocal images indicate the UP pore is completely blocked, whereas the UPS pore is not, especially further downgradient from the inlet. These results indicate that tracer breakthrough across the micromodel centerline occurs when precipitates exist as isolated crystals that do not connect across a pore body, and that faster precipitation (e.g., faster precipitation in UP compared to UPS) results in more complete pore blockage along the length of the micromodel. A primary concern of pore blockage is that mixing will be restricted, and this will limit the extent of mineral precipitation that occurs in the subsurface. It is also possible that pore blockage will decrease because precipitates will dissolve due to undersaturation of the surrounding fluid [*Tartakovsky et al.*, 2008; *Katz et al.*, 2011; *Zhang et al.*, 2010; *Yoon et al.*, 2012].

4. Conclusions

[35] We determined from pore-scale experiments and spectroscopic evaluation that uranium and phosphate, each at 100 μ*M*, will mix transverse to flow and react to form only chernikovite in a time scale of hours to days, even in the presence of Ca^{2+} and SO_4^{2-}. We also determined that the presence of Ca^{2+} and SO_4^{2-} affects the rate of precipitation, but only within a factor of three, and the shape and size of crystals formed. However, EDXS results indicate that Ca and S are not incorporated into the chernikovite lattice. We determined from pore-scale modeling that chernikovite is the least favored mineral to precipitate and that UOP and Ca-autunite are the most favored. Consistent with literature results, it appears that chernikovite is kinetically favored during the time scale (hours to days) of our study. Last, we determined that rapid chernikovite precipitation blocks pores and diverts flow. In the field, rapid chernikovite precipitation and flow diversion are possible when phosphate is amended to groundwater. Permeability changes were observed at the Hanford area 300 site after phosphate addition [*Vermeul et al.*, 2009], and this was attributed to hydroxyapatite precipitation. Our results suggest that pore blockage due to chernikovite precipitation may also be occurring and adversely affecting mixing and continued precipitation of U(VI). Further work is required to evaluate the extent of uranium that can be sequestered in the field with phosphate addition, the prevailing mineralogy at longer time scales, and the stability of precipitated uranium minerals when phosphate addition is discontinued.

Appendix A

[36] In Appendix A, the supplemental information includes a plot of cumulative frequency distributions for individual crystal areas in the UP, UCaP, and UPS systems (Figure A1), a list of speciation reactions and stability constants used in this work (Table A1), and minerals and their solubility products available in the literature (Table A2).

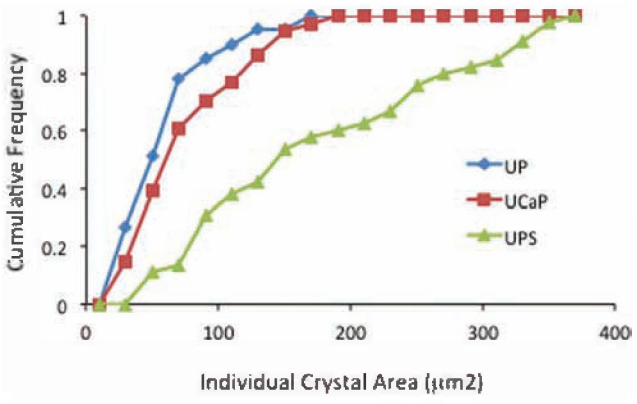

Figure A1. Cumulative frequency distribution of individual crystal areas.

Table A1. Speciation Reactions and Stability Constants

Reaction	log K[a]
Uranium Species	
$UO_2^{2+}+H_2O=UO_2OH^++H^+$	−5.25
$UO_2^{2+}+2H_2O=UO_2(OH)_{2(aq)}+2H^+$	−12.15
$UO_2^{2+}+3H_2O=UO_2(OH)_3^-+3H^+$	−20.25
$UO_2^{2+}+4H_2O=UO_2(OH)_4^{2-}+4H^+$	−32.40
$2UO_2^{2+}+H_2O=(UO_2)_2OH^{3+}+H^+$	−2.70
$2UO_2^{2+}+2H_2O=(UO_2)_2(OH)_2^{2+}+2H^+$	−5.62
$3UO_2^{2+}+4H_2O=(UO_2)_3(OH)_4^{2+}+4H^+$	−11.90
$3UO_2^{2+}+5H_2O=(UO_2)_3(OH)_5^++5H^+$	−15.55
$3UO_2^{2+}+7H_2O=(UO_2)_3(OH)_7^-+7H^+$	−32.20
$4UO_2^{2+}+7H_2O=(UO_2)_4(OH)_7^++7H^+$	−21.90
$UO_2^{2+}+PO_4^{3-}=UO_2PO_4^-$	13.23
$UO_2^{2+}+PO_4^{3-}+H^+=UO_2HPO_{4(aq)}$	19.59
$UO_2^{2+}+PO_4^{3-}+2H^+=UO_2H_2PO_4^+$	22.82
$UO_2^{2+}+PO_4^{3-}+3H^+=UO_2H_3PO_4^{2+}$	22.46
$UO_2^{2+}+2PO_4^{3-}+4H^+=UO_2(H_2PO_4)_{2(aq)}$	44.04
$UO_2^{2+}+2PO_4^{3-}+5H^+=UO_2(H_2PO_4)(H_3PO_4)^+$	45.05
$UO_2^{2+}+CO_3^{2-}=UO_2CO_{3(aq)}$	9.94
$UO_2^{2+}+2CO_3^{2-}=UO_2(CO_3)_2^{2-}$	16.61
$UO_2^{2+}+3CO_3^{2-}=UO_2(CO_3)_3^{4-}$	21.84
$3UO_2^{2+}+6CO_3^{2-}=(UO_2)_3(CO_3)_6^{6-}$	54.00
$2UO_2^{2+}+CO_3^{2-}+3H_2O=(UO_2)_2CO_3(OH)_3^-+3H^+$	−0.85
$3UO_2^{2+}+CO_3^{2-}+3H_2O=(UO_2)_3CO_3(OH)_3^++3H^+$	0.66
$UO_2^{2+}+NO_3^-=UO_2NO_3^+$	0.3
$Ca^{2+}+UO_2^{2+}+3CO_3^{2-}=CaUO_2(CO_3)_3^{2-}$	27.18[b]
$2Ca^{2+}+UO_2^{2+}+3CO_3^{2-}=Ca_2UO_2(CO_3)_{3(aq)}$	30.7[b]
$UO_2^{2+}+SO_4^{2-}=UO_2(SO_4)_{(aq)}$	3.15
$UO_2^{2+}+2SO_4^{2-}=UO_2(SO_4)_2^{2-}$	4.14
Other Species	
$Ca^{2+}+PO_4^{3-}=CaPO_4^-$	6.46[c]
$Ca^{2+}+PO_4^{3-}+H^+=CaHPO_{4(aq)}$	15.09[c]
$Ca^{2+}+PO_4^{3-}+2H^+=CaH_2PO_4^+$	20.96[c]
$Na^++PO_4^{3-}+H^+=NaHPO_4^-$	13.45[c]
$Na^++CO_3^{2-}=NaCO_3^-$	1.27
$Na^++CO_3^{2-}+H^+=NaHCO_{3(aq)}$	10.08
$Na^++SO_4^{2-}=NaSO_4^-$	0.70
$CO_3^{2-}+H^+=HCO_3^-$	10.33[c]
$CO_3^{2-}+2H^+=H_2CO_{3(aq)}$	16.68[c]
$PO_4^{3-}+H^+=HPO_4^{2-}$	12.35
$PO_4^{3-}+2H^+=H_2PO_4^-$	19.56
$PO_4^{3-}+3H^+=H_3PO_{4(aq)}$	21.70
$SO_4^{2-}+H^+=HSO_4^-$	1.99
$H_2O=H^++OH^-$	−14.00[c]

[a]From *Guillaumont and Mompean* [2003] unless otherwise noted.
[b]*Dong and Brooks* [2006].
[c]*Martell and Smith* [2001].

Table A2. Minerals and Their Solubility Products at 298 K and I=0 M

Reaction	Name	log K_{sp} Reference Value	log K_{sp} Other Values
$UO_2HPO_4 \cdot 4H_2O_{(s)}=UO_2^{2+}+PO_4^{3-}+H^+ +4H_2O$	Chernikovite	−24.20[a]	−25.1[b]
$UO_2HPO_4 \cdot 3H_2O_{(s)}=UO_2^{2+}+PO_4^{3-}+H^+ +3H_2O$	UHP	−25.52[c]	−0.11/+0.07[c]
$(UO_2)_3(PO_4)_2 \cdot 4H_2O_{(s)}=3UO_2^{2+}+2PO_4^{3-}+4H_2O$	UOP	−49.36[a]	−0.04/+0.02[c]
$NaUO_2PO_4 \cdot xH_2O_{(s)}=UO_2^{2+}+Na^+ +PO_4^{3-}+xH_2O$	Na meta-autunite	−23.64[a]	
$Ca(UO_2)_2(PO_4)_2 \cdot 3H_2O_{(s)}=2UO_2^{2+}+Ca^{2+}+2PO_4^{3-}+3H_2O$	Ca meta-autunite	−48.36[c]	±0.03[c]
$UO_3 \cdot 2H_2O_{(s)}+2H^+=UO_2^{2+}+3H_2O$	Metaschoepite	5.6[d]	
$Ca(PO_4)_3OH_{(s)}=5Ca^{2+}+3PO_4^{3-}+OH^-$	HAP	−53.28[e]	−58.0[f]

[a] *Grenthe et al.* [1992].
[b] *Johnson* [2000].
[c] *Gorman-Lewis et al.* [2009]. Plus or minus two standard deviations from experimental data were used to compute maximum SR values.
[d] *Gorman-Lewis et al.* [2008b].
[e] *Zhu et al.* [2009].
[f] *Valsami-Jones et al.* [1998].

[37] **Acknowledgments.** We thank Bruce Arey at the EMSL PNNL for help with SEM and EDS. We also thank Thomas Johnson and Craig Lundstrom at the University of Illinois at Urbana-Champaign for helpful suggestions regarding SEM and EDXS analyses. This work was supported by the Environmental Remediation Science Program (ERSP), DOE, grant DE-SC0001280. Support for MFF was also provided by a University of Illinois Graduate Student Fellowship. A portion of these experiments were conducted in the William R. Wiley Environmental Molecular Sciences Laboratory, a U.S. DOE national scientific user facility sponsored by the DOE's Office of Biological and Environmental Research and located at PNNL. H.Y. is supported as part of the Center for Frontiers of Subsurface Energy Security, an Energy Frontier Research Center funded by the DOE, Office of Science, Office of Basic Energy Sciences under award DE-SC0001114. Sandia National Laboratories is a multiprogram laboratory managed and operated by Sandia Corporation, a wholly owned subsidiary of Lockheed Martin Corporation, for the DOE's National Nuclear Security Administration under contract DE-AC04-94AL85000.

References

Arai, Y., M. A. Marcus, N. Tamura, J. A. Davis, and J. M. Zachara (2007), Spectroscopic evidence for uranium bearing precipitates in vadose zone sediments at the Hanford 300-Area site, *Environ. Sci. Technol.*, *41*, 4633–4639.

Arey, J. S., J. C. Seaman, and P. M. Bertsch (1999), Immobilization of uranium in contaminated sediments by hydroxyapatite addition, *Environ. Sci. Technol.*, *33*, 337–342.

Beazley, M. J., R. J. Martinez, P. A. Sobecky, S. M. Webb, and M. Taillefert (2009), Nonreductive biomineralization of uranium(VI) phosphate via microbial phosphatase activity in anaerobic conditions, *Geomicrobiol. J.*, *26*, 431–441.

Bernhard, G., G. Geipel, T. Reich, V. Brendler, S. Amayri, and H. Nitsche (2001), Uranyl (VI) carbonate complex formation: Validation of the $Ca_2UO_2(CO_3)_{3(aq)}$ species. *Radiochim. Acta*, *89*, 511–518.

Bethke, C. M. and S. Yeakel (2009), *The Geochemist's Workbench®, Version 8.0: GWB Essentials Guide, Hydrogeology Program*, 84 pp., Univ. of Ill., Urbana.

Bostick, W. D., R. J. Stevenson, L. A. Harris, E. Peery, J. R. Hall, J. L. Shoemaker, R. J. Jarabek, and E. B. Munday (2003), Use of apatite for chemical stabilization of subsurface contaminants final report, *Final Rep. DE-AC26-01NT41306*, U.S. Dep. of Energy, May.

Cao, X., W. G. Harris, M. S. Josan, and V. D. Nair (2007), Inhibition of calcium phosphate precipitation under environmentally-relevant conditions, *Sci. Total Environ.*, *383*(1–3), 205–215.

Castro, F., A. Ferreira, F. Rocha, A. Vicente, and J. A. Teixeira (2012), Characterization of intermediate stages in the precipitation of hydroxyapatite at 37 °C, *Chem. Eng. Sci.*, *77*(30), 150–156.

Catalano, J. G., S. M. Heald, J. M. Zachara, and G. R. Brown, Jr. (2004), Spectroscopic and diffraction study of uranium speciation in contaminate vadose zone sediments from the Hanford Site, Washington State, *Environ. Sci. Technol.*, *38*, 2822–2828.

Chomsurin, C., and C. J. Werth (2003), Analysis of pore-scale nonaqueous phase liquid dissolution in etched silicon pore networks. *Water Resour. Res.*, *39*(9), 1265–1276, doi:10.1029/2002WR001643.

Dong, W., and S. C. Brooks (2006), Determination of the formation constants of ternary complexes of uranyl and carbonate with alkaline earth metals (Mg^{2+}, Ca^{2+}, Sr^{2+}, and Ba^{2+}) using anion exchange method, *Environ. Sci. Technol.*, *40*, 4689–4695.

Dorhout, P. K., R. J. Kissane, K. D. Abney, L. R. Avens, P. G. Eller, and A. B. Ellis (1989), Intercalation reaction of the neptunyl(VI) dication with hydrogen uranyl phosphate and hydrogen neptunyl phosphate host lattices, *Inorg. Chem. 28*, 2929–2930.

Dunham-Cheatham, S., X. Rui, B. Bunker, N. Menguy, R. Hellmann, and J. Fein (2011), The effects of non-metabolizing bacterial cells on the precipitation of U, Pb, and Ca phosphates, *Geochim. Cosmochim. Acta*, *75*, 2828–2847.

Fang, Y., S. B. Yabusaki, S. J. Morrison, J. P. Amonette, and P. E. Long (2009), Multicomponent reactive transport modeling of uranium bioremediation field experiments, *Geochim. Cosmochim. Acta*, *73*(20), 6029–6051.

Frost, R. L., J. Cejka, M. L. Weier, W. N. Martens, and G. A. Ayoko (2007), Raman spectroscopy of uranopilite of different origins—Implications for molecular structure, *J. Raman Spectrosc.*, *38*, 398–409.

Fuller, C. C., J. R. Bargar, J. A. Davis, and M. J. Piana (2002), Mechanisms of uranium interactions with hydroxyapatite: Implications for groundwater remediation, *Environ. Sci. Technol.*, *36*(2), 158–165.

Fuller, C. C., J. R. Bargar, and J. A. Davis (2003), Molecular scale characterization of uranium sorption by bone apatite materials for a permeable reactive barrier demonstration, *Environ. Sci. Technol.*, *37*, 4642–4649.

Gabriel, U., J. P. Gaudet, L. Spadini, and L. Charlet (1998), Reactive transport of uranyl in a goethite column: An experimental and modelling study, *Chem. Geol.*, *151*(1–4), 107–128.

Gorman-Lewis, D., P. C. Burns, and J. B. Fein (2008a), Review of uranyl mineral solubility measurements, *J. Chem. Thermodyn.*, *40*(3), 335–352.

Gorman-Lewis, D., J. B. Fein, P. C. Burns, J. E. S. Szymanowski, and J. Converse (2008b), Solubility measurements of the uranyl oxide hydrate phases metaschoepite, compreignacite, Na-compreignacite, becquerelite, and clarkeite, *J Chem. Thermodyn.*, *40*(6), 980–990.

Gorman-Lewis, D., T. Shvareva, K. Kubatko, P. C. Burns, D. M. Wellman, B. McNamara, A. Szymanowski, and J. B. Fein (2009), Thermodynamic properties of autunite, uranyl hydrogen phosphate, and uranyl orthophosphate for solubility and calorimetric measurements, *Environ. Sci. Technol.*, *43*, 7416–7422.

Grenthe, I., J. Fuger, R. J. M. Konings, R. J. Lemire, A. B. Mueller, C. Nguyen-Trung, and H. Wanner (1992), *Chemical Thermodynamics of Uranium*, Elsevier, Amsterdam.

Guillaumont, R., and F. J. Mompean (2003), *Update on the Chemical Thermodynamics of Uranium, Neptunium, Plutonium, Americium and Technetium*, Elsevier and OECD Nucl. Energy Agency, Organ. for Econ. Co-op. and Dev., Amsterdam.

Helgeson, H. C., and D. H. Kirkham (1974), Theoretical prediction of the thermodynamic behavior of aqueous electrolytes at high pressures and temperatures: II. Debye-Hückel parameters for activity coefficients and relative partial molal properties, *Am. J. Sci.*, *274*(10), 1199–1261.

Helgeson, H. C., D. H. Kirkham, and G. C. Flowers (1981), Theoretical prediction of the thermodynamic behavior of aqueous electrolytes by high pressures and temperatures: IV. Calculation of activity coefficients, osmotic coefficients, and apparent molal and standard and relative partial molal properties to 600 degrees C and 5kb, *Am. J. Sci.*, *281*, 1249–1516.

Hiemstra, T., W. H. Van Riemsdijk, A. Rossberg, and K. U. Ulrich (2009), A surface structural model for ferrihydrite: II. Adsorption of uranyl and carbonate, *Geochim. Cosmochim. Acta*, *73*, 4437–4451.

Jerden, J. L., and A. K. Sinha (2003), Phosphate based immobilization of uranium in an oxidizing bedrock aquifer, *Appl. Geochem.*, *18*(6), 823–843.

Jerden, J. L., and A. K. Sinha (2006), Geochemical coupling of uranium and phosphorus in overlying an unmined uranium deposit: Coles Hill, Virginia, *J. Geochem. Explor.*, *91*, 56–70.

Jerden, J. L., A. K. Sinha, and L. Zelazny (2003), Natural immobilization of uranium by phosphate mineralization in an oxidizing saprolite-soil profile: Chemical weathering of the Coles Hill uranium deposit, Virginia, *Chem. Geol.*, *199*, 129–157.

Johnson, J. (2000), Geochemist's Workbench, Database thermo.com, *V8.R6. 230*, Lawrence Livermore National Laboratory, Livermore, Calif.

Katz, G. E., B. Berkowitz, A. Guadagnini, M. W. Saaltink (2011), Experimental and modeling investigation of multicomponent reactive transport in porous media, *J. Contam. Hydrol.*, *120/121*, 27–44, doi:10.1016/j.jconhyd.2009.11.002.

Knutson, C., C. J. Werth, and A. J. Valocchi (2005), Pore scale simulations of biomass growth along the transverse mixing zone of a model 2D porous medium, *Water Resour. Res.*, *41*, W07007, doi:10.1029/2004WR003459.

Lerman, A. (1979), *Geochemical Processes: Water and Sediment Environments*, 481 pp., Wiley, New York.

Lichtner, P. C. (1985), Continuum model for simultaneous chemical reactions and mass transport in hydrothermal systems, *Geochim. Cosmochim. Acta*, *49*(3), 779–800.

Liu, C., J. Shang, and J. M. Zachara (2011), Multispecies diffusion models: A study of uranyl species diffusion, *Water Resources Res.*, *47*, W12514, doi:10.1029/2011WR010575.

Martell, A. E., and R. M. Smith (2001), NIST Critically selected stability constants of metal complexes, Version 6.0, NIST Standard Reference Database 46, National Institute of Standards and Technology, Gaithersburg, MD.

Martinez, R. J., M. J. Beazley, M. Taillefert, A. K. Arakaki, J. Skolnick, and P. A. Sobecky (2007) Aerobic uranium(VI) bioprecipitation by metal-resistant bacteria isolated from radionuclide and metal-contaminated subsurface soils, *Environ. Microbiol.*, *9*, 3122–3133.

Moody, T. E., S. W. Petersen, E. G. Torne, J. Vlcakova, and J. F. Higginbotham (1996), Laboratory scale stabilization of N-springs groundwater strontium-90 using phosphatic materials, Report BHI-00864, Bechtel Hanford, Inc., Richland, Wash.

Morosin, B. (1978), Hydrogen uranyl phosphate tetrahydrate, a hydrogen ion solid electrolyte, *Acta Cryst.*, *B34*, 3732–3734.

Morrison, S. J., and R. R. Spangler (1992), Extraction of uranium and molybdenum from aqueous solutions: A survey of industrial materials for use in chemical barriers for uranium mill tailings, *Environ. Sci. Technol.*, *26*(10), 1922–1931.

Murakami, T., T. Ohnuki, H. Isobe, and T. Sato (1997), Mobility of uranium during weathering, *Am. Mineral.*, *82*, 888–899.

Murakami, T., T. Sato, T. Ohnuki, and H. Isobe (2005), Field evidence for uranium nanocrystallization and its implications for uranium transport, *Chem. Geol.*, *221*, 117–126.

Naftz, D. L., G. W. Freethey, W. F. Holmes, and R. C. Rowland (1996), Field demonstration of in situ chemical barriers to control uranium contamination in ground water, Fry Canyon, Utah, Proj. *UT-96–242, U.S. Geol. Surv.*, Water Resour. of Utah, Salt Lake City.

Nair, S., and B. J. Merkel (2011), Impact of alkaline earth metals on aqueous speciation of uranium(VI) and sorption on quartz, *Aquat. Geochem.*, *17*, 209–219.

National Research Council (NRC) (2008), *Review of the Toxicologic and Radiologic Risks to Military Personnel From Exposures to Depleted Uranium During and After Combat*, Natl. Acad. Press, Washington, D. C.

National Research Council (NRC) (2010), *Science and Technology for DOE Site Cleanup: Workshop Summary*, Natl. Acad. Press, Washington, D. C.

Otsu, N. (1979), A threshold selection method from gray-level histograms, *IEEE Trans. Syst. Man Cybern.*, *9*, 62–66.

Rasband, W. S. (1997–2011), *ImageJ*, U. S. Natl. Inst. of Health, Bethesda, Md., USA. [Available at http://imagej.nih.gov/ij/.].

Schecher, W. D., and D. C. McAvoy (1999), *MINEQL+: A Chemical Equilibrium Modeling System*, Environ. Res. Software, Hallowell, M. E.

Simon, F. G., and V. Biermann (2005), Chapter 4. Behaviour of uranium in elemental iron and hydroxyapatite reactive barriers: Column experiments, In *Long-Term Performance of Permeable Reactive Barriers,* vol. 7, *Trace Metals and Other Contaminants in the Environment*, edited by K. E. Roehl et al., pp. 77–109, Elsevier, San Diego, Calif.

Simon, F. G., V. Biermann, and B. Peplinski (2008), Uranium removal from groundwater using hydroxyapatite, *Appl. Geochem.*, *23*, 2137–2145.

Singh, A., K. U. Ulrich, and D. E. Giammar (2010), Impact of phosphate on U(VI) immobilization in the presence of goethite, *Geochim. Cosmochim. Acta*, *74*, 6324–6343.

Sowder, A. G. (1998), Assessing the impact of uranyl mineralogy in the U-Ca-PO_4 system on the environmental availability of uranium, Ph.D. dissertation, Clemson Univ., Clemson, S. C.

Sowder, A. G., S. B. Clark, and R. A. Fjeld (1996), The effect of silica and phosphate on the transformation of schoepite to becquerelite and other uranyl phases, *Radiochim. Acta*, *74*, 45–49.

Sowder, A. G., S. B. Clark, and R. A. Fjeld (2001), The impact of mineralogy in the U(VI)-Ca-PO_4 system on the environmental availability of uranium. *J. Radioanal. Nucl. Chem.*, *248*, 517–524.

Tartakovsky, A. M., G. Redden, P. C. Lichtner, T. D. Scheibe, and P. Meakin (2008), Mixing-induced precipitation: Experimental study and multiscale numerical analysis, *Water Resour. Res.*, *44*, W06S04, doi:10.1029/2006WR005725.

Um, W. Y., J. P. Icenhower, C. F. Brown, R. J. Serne, Z. M. Wang, C. J. Dodge, and A. J. Francis (2010), Characterization of uranium-containing sediments from beneath a nuclear waste storage tank from Hanford, Washington: Implication for contaminant transport and fate, *Geochim. Cosmochim. Acta*, *74*, 1363–1380.

United States Environmental Protection Agency (USEPA) (2000), Field demonstration of permeable reactive barriers to remove dissolved uranium from groundwater, Fry Canyon, Utah, EPA 402-C-00-001, Washington, DC, November.

U.S. Department of Energy (DOE) (1992), Alternatives to land disposal of solid radioactive mixed wastes on the Hanford Site, DOE/RL-92-22, U.S. Department of Energy, Richland Operations Office, Richland, Wash.

Valsami-Jones, E., K. W. Ragnarsdottir, A. Putnis, D. Bosbach, A. J. Kemp, and G. Cressey (1998), Solubility and ion activity products of calcium phosphate minerals, *Chem. Geol.*, *151*, 215–233.

Van Haverbeke, L., R. Vochten, and K. Van Springel (1996), Solubility and spectrochemical characteristics of synthetic chernikovite and meta-ankoleite, *Miner. Mag.*, *60*(402), 759–766.

Van Kemenade, M. J. J. M., and P. L. De Bruyn (1987), A kinetic study of precipitation from supersaturated calcium phosphate solutions, *J. Colloid Interface. Sci.*, *118*, 564–585.

Vermeul, V. R., B. N. Bjornstad, B. G. Fritz, J. S. Fruchter, D. P. Mendoza, D. R. Newcomer, M. L. Rockhold, D. M. Wellman, and M. D. Williams (2009), 300 area uranium stabilization through polyphosphate injection, *PNNL-18529*, Pac. Northwest Natl. Lab., Richland, Wash.

Vermeul, V. R., M. D. Williams, B. G. Fritz, R. D. Mackley, D. P. Mendoza, D. R. Newcomer, M. L. Rockhold, B. A. Williams, and D. M. Wellman (2007), Treatability test plan for 300 area uranium stabilization through polyphosphate injection, PNNL-16571, Pac. Northwest Natl. Lab., Richland, Wash.

Wellman, D. M., J. G. Catalano, J. P. Icenhower, and A. P. Gamerdinger (2005), Synthesis and characterization of sodium meta-autunite, $Na[UO_2PO_4]\cdot 3H_2O$, *Radiochim. Acta*, *93*(7), 393–399.

Wellman, D. M., E. M. Pierce, E. L. Richards, B. C. Butler, K. E. Parker, J. N. Glovack, S. D. Burton, S. R. Baum, E. T. Clayton, and E. A. Rodriguez (2007), 300 area uranium plume treatability demonstration project, PNNL-16683, Pac. Northwest Natl. Lab., Richland, Wash.

Wellman, D. M., J. N. Glovack, K. Parker, E. L. Richards, and E. M. Pierce, (2008), Sequestration and retention of uranium(VI) in the presence of hydroxyapatite under dynamic geochemical conditions, *Environ. Chem.*, *5*, 40–50.

Willingham, T. W., C. J. Werth, and A. J. Valocchi (2008), Evaluation of the effects of porous media structure on mixing-controlled reactions using pore-scale modeling and micromodel experiments, *Environ. Sci. Technol.*, *42*, 3185–3193.

Willingham, T., C. Zhang, C. J. Werth, A. J. Valocchi, M. Oostrom, and T. W. Wiestma (2010), Using dispersivity values to quantify the effects of

pore-scale flow focusing on enhanced reaction along transverse mixing zone, *Adv. Water Res.*, *33*, 525–535.

Wolbarst, A. B., et al. (1999), Sites in the United States contaminated with radioactivity. *Health Phys.*, *77*, 247–260.

Wolery, T. J. (1992), EQ3/6, *A Software Package for Geochemical Modeling of Aqueous Systems. Version 7.0*, Lawrence Livermore Natl. Lab./ Univ. of Livermore, Calif.

Wu, W. M., et al. (2006), Pilot-scale in situ bioremediation of uranium in a highly contaminated aquifer: 1. Conditioning of a treatment zone, *Environ. Sci. Technol.*, *40*, 3978–3985.

Yoon, H., A. J. Valocchi, C. J. Werth, and T. Dewers (2012), Pore-scale simulation of mixing-induced calcium carbonate precipitation and dissolution in a microfluidic pore network, *Water Resour. Res.*, *48*, W02524, doi:10.1029/2011WR011192.

Zachara, J. M., J. A. Davis, J. P. McKinley, D. M. Wellman, C. Liu, N. Qafoku, and S. B. Yabusaki (2005), Uranium geochemistry in vadose zone and aquifer sediments from the 300 area uranium plume, *PNNL-15121*, Pac. Northwest Natl. Lab., Richland, Wash.

Zhang, C. Y., K. Dehoff, N. Hess, M. Oostrom, T. W. Wietsma, A. J. Valocchi, B. W. Fouke, and C. J. Werth (2010), Pore-scale study of transverse mixing induced $CaCO_3$ precipitation and permeability reduction in a model subsurface sedimentary system, *Environ. Sci. Technol.*, *44*, 7833–7838.

Zhu, Y., X. Zhang, Y. Chen, Q. Xie, J. Lan, M. Qian, and N. He (2009), A comparative study on the dissolution and solubility of hydroxylapatite and fluorapatite at 25°C and 45°C, *Chem. Geol.*, *268*, 89–96.

Zimmerman, K. L., D. S. Barber, M. F. Ehrich, L. Tobias, S. Hancock, J. Hinckley, E. M. Binder, and B. S. Jortner (2007), Temporal clinical chemistry and microscopic renal effects following acute uranyl acetate exposure, *Toxicol. Pathol.*, *35*, 1000–1009.